

Type 1 AGN at low z . III. The optical narrow line ratios

Jonathan Stern* and Ari Laor*

Department of Physics, Technion – Israel Institute of Technology, Haifa 32000, Israel

25 October 2012

ABSTRACT

We present the optical narrow line ratios in an SDSS based sample of 3 175 broad $H\alpha$ selected type 1 AGN, and explore their positions in the BPT diagrams as a function of the AGN and the host properties. We find the following: 1. The luminosities of all measured narrow lines ($H\alpha$, $H\beta$, $[O\ III]$, $[N\ II]$, $[S\ II]$, $[O\ I]$) show a Baldwin relation relative to the broad $H\alpha$ luminosity $L_{bH\alpha}$, with slopes in the range of $0.53 - 0.72$. 2. About 20% of the type 1 AGN reside within the ‘Composite’ and ‘SF’ regions of the BPT diagrams. These objects also show excess narrow $H\alpha$ and UV luminosities, for their $L_{bH\alpha}$, consistent with contribution from star formation which dominates the narrow lines emission, as expected from their positions in the BPT diagrams. 3. The type 1 which reside within the AGN region in the BPT diagrams, are offset to lower $[S\ II]/H\alpha$ and $[N\ II]/H\alpha$ luminosity ratios, compared to type 2 AGN. This offset is a selection effect, related to the lower AGN/host luminosity selection of the type 2 AGN selected from the SDSS galaxy sample. 4. The $[N\ II]/H\alpha$ and $[N\ II]/[S\ II]$ ratios in type 1 AGN increase with the host mass, as expected if the mass-metallicity relation of quiescent galaxies holds for the AGN narrow line region. 5. The broad lines optical Fe II is higher for a higher $[N\ II]/H\alpha$, at a fixed L_{bol} and Eddington ratio L/L_{Edd} . This suggests that the broad line region metallicity is also related to the host mass. 6. The fraction of AGN which are LINERs increases sharply with decreasing L/L_{Edd} . This fraction is the same for type 1 and type 2 AGN. 7. The BPT position is unaffected by the amount of dust extinction of the optical-UV continuum, which suggests the extinguishing dust resides on scales larger than the NLR.

Key words:

1 INTRODUCTION

The gas located on $1 - 1000$ pc scale from the center of Active Galactic Nuclei (AGN) plays a role in several important processes, which are not well understood. This gas is the source of AGN fuel, and may absorb AGN energy and momentum output, thus potentially coupling the growth of the bulge with the growth of the central black hole. It is enriched during the life cycle of stars near the nucleus, and therefore traces the star formation history. It also re-processes the AGN ionization continuum, which originates from a few Schwarzschild radii, and thus its emission may allow to constrain the accretion mode in the innermost regions.

The most prominent optical signature of the circumnuclear gas in AGN is its emission lines, which have widths typical of the galaxy potential (~ 300 km s $^{-1}$). These lines are known as the narrow emission lines, and the emitting region as the narrow line region (NLR). The vast majority of NLR analyses were performed on type 2 AGN where the central source is obscured, partly because the narrow lines are not blended with the broad emission lines, which dominate the emission features in unobscured type 1 AGN. Previous studies of the NLR of type 1 AGN were either lim-

ited to the most prominent forbidden lines (e.g. Boroson & Green 1992, using $[O\ III]\ \lambda 5007$), limited to small samples (e.g. Baldwin, Phillips & Terlevich 1981, hereafter BPT, Cohen 1983, Ho et al. 1997b, Rodríguez-Ardila et al. 2000, Véron-Cetty et al. 2001, Dietrich et al. 2005), or limited to samples of very weak type 1 AGN (e.g. Greene & Ho 2007) in which the narrow lines become more prominent (Stern & Laor 2012b, hereafter Paper II).

Here we provide the first study of the NLR properties of a large sample of 3 175 type 1 AGN, defined in Stern & Laor (2012a, hereafter Paper I) with minor adjustments below. The T1 samples spans a black hole mass range of $10^6 < M_{BH} < 10^{9.5} M_{\odot}$ and a bolometric luminosity range of $10^{42} < L_{bol} < 10^{46}$ erg s $^{-1}$. In contrast with earlier studies of type 2 AGN, here the innermost AGN is directly observed. We use the narrow line measurements, combined with the AGN SED and broad line measurements, to address the following questions:

How complete is the BPT classification of AGN? The BPT diagrams (BPT and Veilleux and Osterbrock 1987, hereafter VO) compare the ratio of the $[O\ III]$ to $H\beta$ luminosity (for brevity $[O\ III]/H\beta$), with $[N\ II]\lambda 6583/H\alpha$, $[S\ II](\lambda\lambda 6716, 6731)/H\alpha$, and $[O\ I](\lambda 6300)/H\alpha$. These line ratios provide a measure of the relative strength of the higher energy ionizing photons, and thus differentiate between stellar and AGN excitation. These diagrams are widely used to define type 2 AGN samples, using separation lines

* E-mail: stern@physics.technion.ac.il (JS);

laor@physics.technion.ac.il (AL)

based on theoretical models (Kewley et al. 2001, hereafter Ke01), and based on the observed distribution of star forming galaxies (Kauffmann et al. 2003, hereafter Ka03).

The BPT/VO AGN selection criteria are commonly viewed as necessary and sufficient conditions to define AGN. However, AGN samples selected by other means show these selection criteria may not be necessary. In a hard X-ray selected sample, a unique signature for AGN emission, Winter et al. (2010) found that five out of 60 objects are in the Star Forming (SFs) galaxies regime, i.e. below the Ka03 line in the [N II]/H α panel of the BPT diagrams, and five more are between the Ka03 line and the Ke01 line, i.e. ‘Composites’. In the $M_{\text{BH}} < 10^{6.2} M_{\odot}$ type 1 sample of Greene & Ho (2007), 39% of the objects are SFs or Composites. This fraction dropped to 18% when the spectra was taken from a narrower slit (Xiao et al. 2011). On the other hand, only 3% of radio loud AGN are classified as Composites or SFs (Buttiglione et al. 2010). Using the T1 sample, which is selected independently of the narrow line properties, we derive the completeness of the BPT-based selection criteria, and its dependence on the AGN emission properties.

How are the properties of the NLR gas related to AGN and host properties? In low z type 2 AGN, the value of [N II]/H α , which follows NLR metallicity, Z_{NLR} , has been found to modestly increase with host mass M_* (Groves et al. 2006) and with host velocity dispersion σ_* (Annibali et al. 2010). These trends are associated with the known $M_* - Z$ relation of quiescent galaxies (Lequeux et al. 1979, and citations thereafter). The $Z_{\text{NLR}} - M_*$ relation is also implied by the fact that most AGN reside in massive galaxies (Ka03) and have $Z_{\text{NLR}} > Z_{\odot}$ (Storchi-Bergmann et al. 1998, Groves et al. 2004, 2006), while the rare low M_* AGN have low Z_{NLR} (Kraemer et al. 1999, Barth et al. 2008; Ludwig et al. 2012). However, these samples are dominated by low L_{bol} AGN, since they are based on the detectability of the host galaxy, and therefore are limited to a small volume where luminous AGN are rare.

In high L_{bol} AGN at high z , an $M_* - Z$ relation can be inferred from the increase of Z_{BLR} with L_{bol} (Hamman & Ferland 1993, 1999, Nagao et al. 2006a), and a likely relation of $L_{\text{bol}} - M_*$. Though Z_{NLR} and Z_{BLR} are related (Shields et al. 2010), there seems to be another variable beyond M_* which determines Z_{BLR} , probably related to the accretion rate in Eddington units (L/L_{Edd} , Shemmer & Netzer 2002, Shemmer et al. 2004, Shields et al. 2010). Therefore, it is interesting to compare Z_{NLR} with L_{bol} directly. Most narrow line measurements in high L_{bol} AGN are based on narrow line radio galaxies samples (De Breuck et al. 2000, Vernet et al. 2001, Iwamuro et al. 2003, Nagao et al. 2006b). These studies measured UV line ratios, except Iwamuro et al. which measured non-BPT optical line ratios. Comparison of NLR properties derived from different lines can be ambiguous, due to degeneracies in the photoionization models (Nagao et al. 2006b). Therefore, the dependence of Z_{NLR} and other NLR properties on L_{bol} is still an open question. In this work we derive indicators of Z_{NLR} based on the BPT ratios, for a large dynamical range in L_{bol} . Using the large size of the T1 sample, we also decouple the dependence of Z_{NLR} on L_{bol} and on M_* , and compare Z_{NLR} with Z_{BLR} .

Is the ratio of UV to X ray luminosity a measure of the slope of the ionizing spectrum? Due to Galactic absorption, the ionizing part of the AGN spectrum in the extreme UV is generally unavailable. Laor et al. (1997) showed that the mean 2 keV luminosity L_X of PG quasars is consistent with an extrapolation of the mean EUV slope (Zheng et al. 1997, Telfer et al. 2002). Therefore, the interpolated slope between L_{UV} and L_X , α_{ox} , may be a good estimate of the true ionizing slope. Since the BPT diagrams provide an inde-

pendent constraint on the ionizing slope, we test this hypothesis by comparing the BPT ratios with α_{ox} in the T1 sample.

A related issue concerns the location of the optically thin dust found in type 1 AGN samples (Richards et al. 2003, Gaskell et al. 2004, Paper I), which can harden α_{ox} . If the extinguishing dust is located within the NLR, the NLR will see a harder spectrum, and the BPT ratios will vary with the amount of reddening. If the extinguishing dust originates from larger scales, the NLR will absorb the original ionizing spectrum, and the BPT ratios will remain constant. Below, we constrain the location of the extinguishing dust using the BPT diagrams.

Is the Seyfert-LINER transition related to other emission properties? Kewley et al. (2006, hereafter Ke06) found a bimodality in the BPT diagrams between high ionization Seyferts and low ionization nuclear emission line regions (LINERs, Heckman 1980). They showed the Seyfert-LINER transition is related to L/L_{Edd} , as noted previously by Ho (2002). This transition has also been claimed to be related to the existence of the broad lines, due to the low detection fraction of broad lines in LINERs (Ho et al. 1997b). We address these suggestions based on the T1 sample.

The paper is organized as follows. In §2.1 – §2.3 we summarize the creation of the T1 sample and the measurement of the AGN and host properties, detailed in Papers I and II. In §2.4 we describe the comparison type 2 sample we use, and account for differences in the measuring procedures. In §3 we extend the relative decrease with L_{bol} (the Baldwin effect) found in Paper II for [O III] and H α , to the H β , [N II], [S II] and [O I] lines, first used here. We then proceed in §4 to measure the BPT ratios of the T1 sample, and their dependence on AGN and host characteristics. In §5, we analyze objects which occupy a region in the BPT plots which is not populated in type 2 samples. Analysis of LINERs and Composites is performed in §6 and §7. In §8 we use the BPT ratios to constrain the AGN ionizing spectrum, and the location of the reddening dust. We summarize our results in §9.

Throughout the paper, we assume a FRW cosmology with $\Omega = 0.3$, $\Lambda = 0.7$ and $H_0 = 70 \text{ km s}^{-1} \text{ Mpc}^{-1}$.

2 THE DATA

2.1 The T1 sample selection

The T1 sample is selected from the 7th data release of the Sloan Digital Sky Survey (SDSS DR7; Abazajian et al. 2009). The SDSS obtained imaging of a quarter of the sky in five bands (*ugriz*; Fukugita et al. 1996) to a 95% *r* band completeness limit of 22.2 mag. Objects are selected for spectroscopy mainly due to their non-stellar colors (Richards et al. 2002), or extended morphology (Strauss et al. 2002). The spectrographs cover the wavelength range 3800Å–9200Å at a resolution of $\sim 150 \text{ km s}^{-1}$, and are flux-calibrated by matching the spectra of simultaneously observed standard stars to their PSF magnitude (Adelman-McCarthy et al. 2008).

We use SDSS spectra which have $0.005 < z < 0.31$ and are classified as quasars or galaxies. To ensure a reliable decomposition of the broad and narrow components of H α , we use only spectra with $S/N > 10$ and a sufficient number of good spectral pixels in the vicinity of H α , as detailed in Paper I. These requirements are fulfilled by 232 837 of the 1.6 million spectra in DR7, named the parent sample. The spectra are corrected for foreground dust, using the maps of Schlegel et al. (1998) and the extinction law of Cardelli et al. (1989). Each spectrum is then fit with three galaxy eigenspectra

Object name	$L_{\text{bH}\alpha}$	Δv	M_*	L_{UV}	α_{ox}	Notes
J000202.95-103037.9	41.9	2310	11.1	43.8	-1.50	-, -, -
J000410.80-104527.2	42.6	1360	11.1	44.6	-1.57	-, -, -
J000611.55+145357.2	42.1	3320	11.2	44.0	-1.57	-, -, -
J000614.36-010847.2	41.6	3910	10.8	43.2	-1.54	-, -, U
J000657.76+152550.0	41.5	3020	10.2	43.0	-1.57	-, -, U

Table 1. The AGN and host characteristics of the T1 sample objects. The values of $L_{\text{bH}\alpha}$ and L_{UV} are in $\log \text{ erg s}^{-1}$, Δv is in km s^{-1} , and M_* is in $\log M_{\odot}$. The last column lists notes for M_* , L_{UV} and L_X , separated by commas: ‘U’ indicates an upper limit, ‘N’ indicates not available, and ‘E’ indicates a large error. The electronic version includes all 3 175 T1 objects.

representing the host (see §2.2.4 below), and a $L_{\lambda} \propto \lambda^{-1.5}$ power law representing the AGN continuum. The host is subtracted, producing a spectrum free of stellar absorption features, excluding the Balmer absorption lines, which are handled at a later stage (see §2.2.4). We also subtract a featureless continuum, derived by interpolating the mean continuum level at 6125Å–6250Å and 6880Å–7000Å. The residual flux at 6250Å–6880Å ($\pm 14,000 \text{ km s}^{-1}$ from H α) is then summed, excluding regions $\pm 690 \text{ km s}^{-1}$ from the [O I] $\lambda\lambda 6300, 6363$, [N II] $\lambda\lambda 6548, 6583$, [S II] $\lambda\lambda 6716, 6731$ and H α narrow emission lines. We find 6986 objects with significant residual flux, which is potentially broad H α emission.

For the objects with significant residual near H α , we fit the profiles of the broad and narrow H α , and the [O III] $\lambda 5007$, [O I], [N II] and [S II] doublets mentioned above. Narrow lines are fit using 4th-order Gauss-Hermite functions (GHs; van der Marel & Franx 1993) and an up to 10th-order GH is used for the broad H α profile. Further details are given in §2.4 of Paper I and §§2.3–2.4 of Paper II. The following criteria are applied to the broad H α fit, in order to exclude objects in which the residual flux is not clearly BLR emission: the FWHM (Δv) of the fit is required to be in the range $1000 - 25000 \text{ km s}^{-1}$; the total flux of the fit, and its flux density at the line centre, are required to be significant. As [O III] and H β are used extensively in this paper, we require them to have a sufficient number of good pixels in their vicinity for the fit to be reliable, as detailed in Paper I.

Of the 3 243 objects that pass these criteria, we use here 3 175 objects in which our algorithm achieved reliable narrow line fits (see below). Due to the small relative number of objects in which the fitting algorithm did not succeed, we do not attempt to improve the algorithm further. The broad H α luminosity ($L_{\text{bH}\alpha}$) and Δv of the 3 175 objects of the T1 sample are listed in Table 1. The selection effects implied by our selection criteria are detailed in Paper I.

2.2 Narrow line measurements

The narrow line luminosities of the T1 sample are listed in Table 2. Below, we address the limitations of our fitting algorithm, which deblends the narrow lines from the broad lines and from the stellar absorption features. The success of the deblending can be further verified with higher S/N spectra, where the transitions between the different components are more prominent. Therefore, we corroborate our results by analyzing mean spectra of different T1 subgroups, which have an effectively higher S/N.

2.2.1 Bad pixels

The main source of bad pixels in the SDSS spectra is poor sky subtraction, which degrades the spectrum mainly at $\lambda > 8000\text{Å}$. There-

fore, the [S II] and [O I] lines are not measurable in 612 (19%) and 190 (6%) of the T1 objects, respectively. These objects are marked in Table 2, and are disregarded in figures where the line is used. Objects in which one of the other lines used in this work has bad pixels do not enter the T1 sample (§2.1).

2.2.2 Upper limits

Our algorithm can robustly detect the six different narrow lines if their mean flux density F_{λ} is 2–3.5 times the local flux density error. The exact value depends on how blended a specific line is with other spectral features, and is listed in Table 3. Upper limits on fluxes of lines with lower F_{λ} are derived by assuming a Gaussian profile, with a flux density equal to the minimum F_{λ} required for detection and the width fit to the other narrow emission lines. Objects with upper limits are noted in Table 2.

The T1 sample detection fractions of the different lines are listed in Table 3. The detection fractions are all $> 77\%$.

2.2.3 [O III]-like narrow lines

As noted in Papers I and II, in 15% of the sample the fit yielded $\text{FWHM}(\text{nH}\alpha) \geq 1.5 \times \text{FWHM}([\text{O III}])$. These objects have non- or barely-detectable narrow lines near H α , and there is no clear transition between the broad and narrow components of the Balmer lines. Therefore, we fit the narrow lines near H α in these objects with a FWHM, 3rd and 4th GH parameters equal to those found for [O III].

An eye-inspection of the narrow H β fits yielded another 188 objects (6%) without a clear NLR/BLR transition, despite having $\text{FWHM} < 1.5 \times \text{FWHM}([\text{O III}])$. We refit these objects with [O III]-like profiles, and updated the relevant narrow line fluxes. The new fit failed on 68 of the objects (reduced $\chi^2 > 2$). Due to their relatively small number, we did not attempt to improve the fit, and simply removed these 68 objects from the sample. This change in the narrow line fluxes of 6% of the T1 sample has a negligible effect on the results presented in Papers I and II.

The narrow H α , H β , and [N II] line fluxes are less certain in objects fit with an [O III]-like profile. Therefore, throughout the paper different symbols are used when these measurements are utilized. These objects are also noted in Table 2.

2.2.4 Strong stellar Balmer absorption

We model the stellar absorption features by fitting the first three Yip et al. (2004) eigenspectra (ESa) to the SDSS spectra, together with a power law for the AGN continuum. Since the Yip et al. ESa have emission lines, in ES1 we replace the lines with the absorption features of the Hao et al. (2005) ES1 (detailed in §2.2 of Paper II). This step is justified since both ES1’s represent an old stellar population. In ES2 and ES3, which represent a younger population, an emission line free ES is not available, so we simply interpolate over the lines.

Since the absorption lines are significantly wider than the emission lines, an interpolation over the emission will not remove the entire absorption feature. However, near H α the interpolation is done also over the [N II] lines which flank H α . Therefore, our fit does not account for the entire H α absorption feature of young stars. In Paper II, we found that in the 5% of the T1 objects that have $L_{\text{nH}\alpha} < 3\text{Å} \times L_{\lambda}(\text{host})$, the $L_{\text{nH}\alpha}$ are underestimated due to improper subtraction of the stellar absorption. Now, the narrow H β

Object name	H β	[O III]	H α	[N II]	[S II]	[O I]	Notes	robust	stellar absorption	BPT-[N II]	BPT-[S II]	BPT-[O I]
J000202.95-103037.9	40.7	41.4	41.5	41.3	41.0	40.2	-, -, -, -, -	+	+	AGN	Seyfert	Seyfert
J000410.80-104527.2	41.3	41.5	41.9	41.6	-1	-1	-, -, -, -, N, N	+	+	Composite	SF	SF
J000611.55+145357.2	40.2	40.6	41.0	40.7	40.5	39.8	-, -, -, -, U	+	+	Composite	SF	Seyfert
J000614.36-010847.2	40.4	40.9	41.1	40.7	-1	39.6	-, -, -, -, N, -	+	+	Composite	SF	SF
J000657.76+152550.0	40.2	40.8	40.7	40.0	40.3	39.7	-, -, -, -, -	+	+	Composite	Seyfert	Seyfert

Table 2. The narrow line measurements of the T1 sample. All luminosities are in $\log \text{ erg s}^{-1}$. Notes on the measurements of the six lines are separated by commas in column 8, ordered as in the table. A ‘U’ designates an upper limit, an ‘N’ designates bad pixels (for [S II] and [O I] only) which are also marked as -1 in the corresponding luminosity. Objects in which the H α , H β , or [N II] narrow line measurements are not robust (§2.2.3), or the Balmer lines are affected by strong stellar absorption features (§2.2.4), are marked by an ‘x’ in the respective following columns. Other objects are marked by a ‘+’. The last three columns list the classification of each object in the corresponding BPT panel. The electronic version includes all 3 175 T1 objects.

Narrow line	λ (Å)	$\min F_{\lambda}/\epsilon_{\lambda}$	Detection Fraction
H β	4961	3	0.84
[O III]	5007	3.5	0.99
[O I]	6300	2.5	0.77
H α	6563	3	0.98
[N II]	6583	3	0.92
[S II]	6716	2.5	0.91
[S II]	6731	2	0.92

Table 3. The detection fractions of the narrow lines used in the paper. Col. 3 notes the minimum flux density required for detection, in units of the local flux density error.

emission line is weaker than H α , and therefore more suspect to significant biases due to improper subtraction of the stellar absorption features. However, near H β the interpolation in ES1 and ES2 is performed only over the narrow H β line, so the wide part of the stellar absorption feature is accounted for by our fit. Therefore we mark the same objects as in Paper II, i.e. objects with $L_{\text{nH}\alpha} < 3\lambda \times L_{\lambda}(\text{host})$, as objects with potentially underestimated $L_{\text{nH}\alpha}$ and $L_{\text{nH}\beta}$. We verify below this suffices in order to identify objects with offset $L_{\text{nH}\beta}$ values.

2.3 Additional Properties

2.3.1 L_* and M_*

We derive the host galaxy luminosity, L_* , by subtracting the estimated net AGN luminosity from the total observed luminosity. For the total observed luminosity we use the SDSS CMODEL flux¹ (Abazajian et al. 2004) in the z -band, which is a linear sum of a de Vaucouleurs model and an exponential model fit to the image, and is the best suited model to account for both the galaxy and the nuclear light. The z -band is chosen since it is the reddest SDSS band, therefore it has the highest host to AGN contrast. It also has the smallest dispersion in the ratio of host mass to host light. We estimate the net AGN luminosity at the z -band, $L_{\text{AGN}; z\text{-band}}$, from $L_{\text{bH}\alpha}$ (Paper I).

To convert L_* to M_* , we use the the median mass to light ratio of $(M/L) = 10^{0.25} (M/L)_{\odot}$, found by Kauffmann et al. (2003b, Fig. 14 there) for galaxies with L_* in the range spanned by the T1 sample. This method has an error of $\sim 50\%$. Since the mass to light ratio is similar for the SDSS- i and z -bands², and all T1 objects have

$z < 0.3$, we do not need to apply a K-correction to L_* when calculating M_* . The individual M_* of the T1 sample objects are listed in Table 1.

An additional source of error is the scatter in the ratio of $L_{\text{AGN}; z\text{-band}}$ to $L_{\text{bH}\alpha}$. We assume this scatter equals the scatter in the relation between $L_{\text{total}; 5100\text{\AA}}$ and $L_{\text{bH}\beta}$ of $0.5 < z < 0.7$ SDSS quasars – the lower z limit ensures the quasars are luminous and host contribution to the continuum is minimal, while the upper z limit ensures H β fully appears in the spectrum. Using the $L_{\text{bH}\beta}$ and $L_{\text{total}; 5100\text{\AA}}$ values from Shen et al. (2011), we find a scatter of 0.2 dex. This scatter implies that in the 9% of the T1 objects with implied $L_{\text{AGN}}/L_* > 1$, the true L_* may be overestimated by a factor of more than 2, while in the 3% of T1s with implied $L_{\text{AGN}}/L_* > 3$, the true L_* may be underestimated by a factor of more than 2. In 0.5% of the objects, the implied L_* is negative. We address these limitations when utilizing L_* and M_* below.

2.3.2 L_{UV} and α_{ox}

We derive the L_{UV} ($\equiv \nu L_{\nu}(1528\text{\AA})$) and L_{X} ($\equiv \nu L_{\nu}(2 \text{ keV})$) of the T1 AGN, from the GALEX (Martin et al. 2005) and ROSAT (Voges et al. 1999) surveys. GALEX observed 89% of the T1s, and detected 93% of them. ROSAT observed the entire sky, and detected 43% of the T1s. The derivation of the luminosities is detailed in Paper II. Table 1 lists L_{UV} and $\alpha_{\text{ox}} \equiv -0.42 \times \log L_{\text{UV}}/L_{\text{X}}$, the slope of the interpolated power law between the UV and the X-ray.

2.4 The T2 sample

We compare our results to the Brinchmann et al. (2004) type 2 AGN sample, which was derived from the SDSS galaxy survey, using the emission lines measurement of the MPA/JHU group³. The type 2 AGN were selected by requiring $S/N > 3$ in the [O III], H β , [N II], and H α narrow emission lines, and being above the Ke01 ‘extreme starburst’ line in the BPT-[N II] panel. We use all type 2 objects that appear in our parent sample (following the $S/N > 10$ and bad pixel cuts, §2.1), excluding the 454 objects which enter the T1 sample, as they show broad H α emission. We name these 13 705 objects as the T2 sample.

The MPA/JHU group modeled the stellar absorption features using the Bruzual and Charlot (2003) stellar library. We use a simpler technique in the T1 sample, based on the Yip et al. (2004) ESa, due to possible degeneracies of different stellar components with the unobscured AGN continuum (see §2.2 in Paper I). In order to understand the effect of the different stellar modeling techniques on

¹ Not available for seven objects. They are disregarded when M_* is used.

² The median (M/L) is larger in the i -band than in the z -band by ~ 0.05 dex, but the normalization is lower by 0.03 dex (Kauffmann et al. 2003b).

³ Available at <http://www.mpa-garching.mpg.de/SDSS/DR7/>

the measured narrow line ratios, and the effect of other differences in the fitting procedure, we run our fitting algorithm on 700 spectra from the T2 sample⁴. Then, we compare the narrow line ratios we measure on these T2s with those published by the MPA/JHU group.

In these 700 type 2s, our algorithm gives [O III]/H β ratios which are on average 0.08 dex larger than the ratios measured by MPA/JHU, with a dispersion of 0.11 dex. Our [N II]/H α , [S II]/H α and [O I]/H α measurements are on average 0.04, 0.1 and 0.07 dex larger than MPA/JHU, with dispersions of 0.09, 0.1, and 0.1 dex. The offsets in the narrow line ratios are mainly due to offsets in the measured flux of the narrow H α and H β lines (mean offset -0.09 dex each), which could imply that we did not fully correct for the stellar Balmer absorption features. Therefore, to minimize offsets originating from measurement issues, we hitherto decrease the narrow line ratios we measure in the T1 sample objects by these mean offsets.

3 THE BALDWIN EFFECT OF THE NARROW LINES

In Figure 1, we present the ratio of the narrow lines luminosity $L_{\text{nH}\beta}$, $L_{\text{[N II]}}$, $L_{\text{[S II]}}$, and $L_{\text{[O I]}}$, with $L_{\text{bH}\alpha}$ as a function of $L_{\text{bH}\alpha}$. Black dots mark objects with robust measurements, while gray markers indicate the less robust values. A trend of decreasing NLR to BLR luminosity ratio with increasing $L_{\text{bH}\alpha}$ is clearly seen for all lines. Similar relations were found in Paper II for [O III] and H α . The least-squares best fit power law slope and associated dispersion are noted in the panels. The relations found in Paper II for [O III] and H α are $L_{\text{nH}\beta} \propto L_{\text{bH}\alpha}^{0.67}$, $\sigma = 0.37$ and $L_{\text{[O III]}} \propto L_{\text{bH}\alpha}^{0.72}$, $\sigma = 0.36$. The formal error on all slopes is ~ 0.01 . We treat $L_{\text{bH}\alpha}$, which is used to select the T1 sample, as the independent variable.

Since $L_{\text{bH}\alpha} \propto L_{\text{bol}}$ (Paper I), the observed trends represent a Baldwin effect (Baldwin 1977) for the narrow lines. Note that the different slopes found above imply some trends in the mean positions with luminosity of the T1 objects in the BPT plots, as shown below.

3.1 Less robust values

In all four panels of Fig. 1, most upper limits fall within the distribution of the general population. The objects in which the narrow lines are fit with an [O III]-like profile (§2.2.3) are located at the high- $L_{\text{bH}\alpha}$ end of the sample. As noted in §2.2.3, the deblending of the Balmer lines and [N II] from the broad lines may be inaccurate in these objects. Indeed, the $L_{\text{[N II]}}/L_{\text{bH}\alpha}$ values of these objects are offset to lower values than the general trend. When excluding these objects, we find $L_{\text{nH}\beta} \propto L_{\text{bH}\alpha}^{0.68}$ and $L_{\text{[N II]}} \propto L_{\text{bH}\alpha}^{0.60}$, i.e. a similar H β slope and a [N II] slope higher by 0.06 compared to when using all objects.

3.2 Comparison with previous studies

Croom et al. (2002) compared the narrow [O III], [O II], [Ne III], and [Ne V] line luminosities with the absolute B magnitudes of 2dF and 6dF quasars (Croom et al. 2001). For a direct comparison with our results we subtract the slope they found for each line with the slope they found for $L_{\text{bH}\beta}$. Comparing the narrow lines to the broad

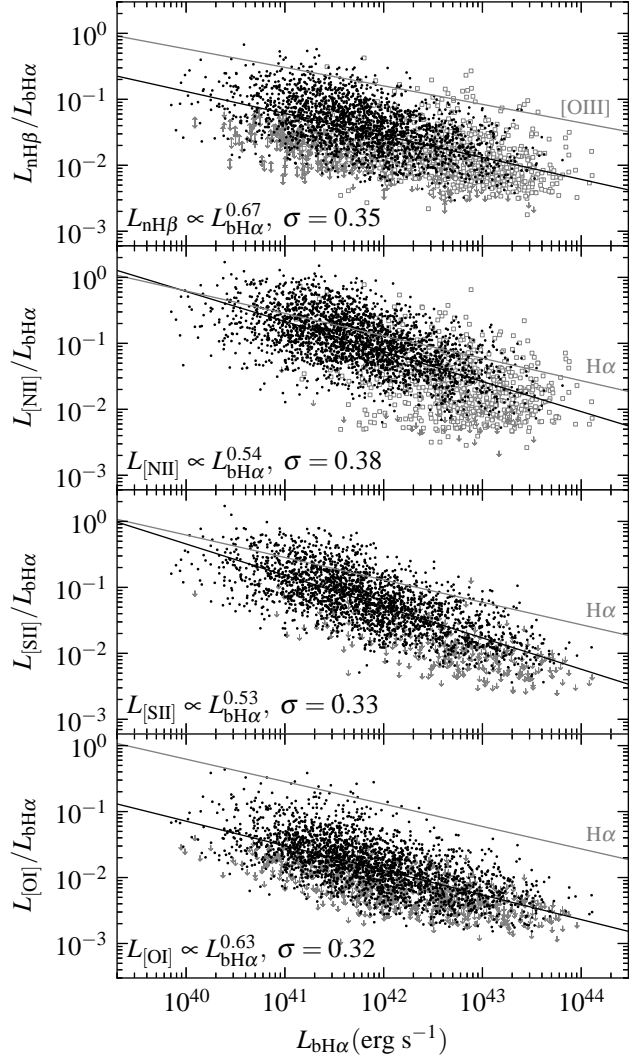


Figure 1. The distribution of $L_{\text{narrow line}}/L_{\text{bH}\alpha}$ versus $L_{\text{bH}\alpha}$ for narrow lines analyzed in the BPT plots below. Robust narrow line measurements are marked by black dots. Profiles of [N II] and H β based on [O III] (§2.2.3) are marked by gray squares. Upper limits (non detections, §2.2.2), and lower limits (stellar absorption for H β only, §2.2.4) are marked by the appropriate arrows. The slope of the best fitting power laws (black lines) and the associated dispersion are noted. For comparison, the relations found in Paper II, for [O III] (index = 0.72) and for H α (index = 0.66), are shown as gray lines. The tendency of increasing NLR / BLR ratio with decreasing $L_{\text{bH}\alpha}$, found in Paper II, is seen in all lines. Since $L_{\text{bH}\alpha} \propto L_{\text{bol}}$ (Paper I), the observed trends represent the Baldwin effect of the narrow lines. When excluding objects marked by squares, the [N II] Baldwin slope increases to 0.60. Note that [S II] and [N II] have steeper slopes than H α , which imply a shift in the mean positions in the BPT plots with luminosity.

H β also avoids the bias created by host contamination of the continuum (Paper II). Their implied slopes are 0.86, 0.49, 0.58 and 0.74 for [O III], [O II], [Ne V], and [Ne III], respectively. All their narrow lines show a Baldwin effect, as found here. Their [O III] slope of 0.86 is steeper than our slope of 0.72, while their [O II] slope of 0.49 is flatter than any of the slopes measured here.

⁴ The first 700 objects, sorted by right ascension.

Mid-IR narrow lines also show Baldwin effects (Hönig et al. 2008, Keremedjiev et al. 2009).

4 THE BPT POSITIONS OF THE T1 AGN

Figure 2 presents the BPT positions of the 3 175 T1 AGN, plotted over the SDSS narrow line galaxies (Fig. 1 from Ke06). Classification lines are from Ke01, Ka03, Ke06 and Ho et al. (1997a, hereafter Ho97). The classification of each T1 object in each panel is listed in Table 2.

The T2 AGN reside, by definition, above the Ke01 line in the BPT-[N II] panel. However, only 80% of the T1 objects reside in the AGN regime, 15% are classified as composite and 5% as SF. We stress again that all T1 AGN are clearly powered by accretion onto a massive black hole, as indicated by the detection of a broad $H\alpha$. Thus, the SDSS type 2 AGN sample is likely only 80% complete. Including composites will increase the completeness to 95%, but may include a significant number of objects which are not true AGN.

We note that the narrow line measurements of two-thirds of the T1s which reside in the SF region are poorly constrained. Thus, with higher quality spectra the true AGN fraction with SF narrow line ratios may therefore be as low as 2%. In comparison, only 18% of the T1s classified as composites and 17% of the T1s classified as ‘AGN’ have poorly-constrained narrow line measurements.

The fraction of T1 which reside outside the AGN region in the BPT-[O I] panel is 18%, and in the BPT-[S II] panel it reaches 29%. The SDSS spectra are taken with a 3'' fiber, which can include a significant fraction of the host galaxy emission. Below we study some indications that the offset from the AGN region in the BPT plots indeed results from host contamination.

Fig. 1 also shows that a sizable fraction of the T1 sample occupies a new region in the BPT panels, with $[O III]/H\beta = 5 - 10$, $[N II]/H\alpha = 0.1 - 0.3$, and $[S II]/H\alpha = 0.1 - 0.3$. These objects have no counterpart in the narrow line sample. Specifically, 10% of T1s with $[O III]/H\beta > 5$ have $[N II]/H\alpha < 0.3$, compared to only 0.8% of the T2 sample. Below, we study the range of AGN and host properties at which these line ratios are dominant, and discuss their physical origin.

In the [O I] panel, 190 objects in the T1 sample are classified as LINER 1s. The vast majority (179) of them appear to the right of the Ho97 line, where the ‘bona-fide’ LINERs reside. This result is consistent with the strong drop in broad $H\alpha$ detection across this line (Ho et al. 1997b, Ho 2008, Wang et al. 2009).

4.1 BPT positions of T1 AGN, by $L_{bH\alpha}$, L/L_{Edd} and L_{AGN}/L_*

In this section we utilize the large size of the T1 sample, and explore their positions within the BPT plots when the sample is cut based on various AGN and host properties. We identify some qualitative trends, which are further explored in the following sections.

Figure 3 presents the BPT positions of the individual T1 objects as a function of $L_{bH\alpha}$, which is a measure of L_{bol} ($= 130 \times L_{bH\alpha}$, Paper I). As in Fig. 2, the positions of the T1s are plotted over the SDSS narrow line galaxies from Ke06. At $\log L_{bH\alpha} = 40.7$ ($L_{bol} = 42.8$), T1 AGN largely overlap the narrow line sample. With increasing luminosity, the T1 AGN shift to lower $[N II]/H\alpha$, lower $[S II]/H\alpha$ values, slightly lower $[O I]/H\alpha$, and higher $[O III]/H\beta$ values, as expected from the different luminosity trends of the different lines (Fig. 1). At quasar luminosities ($\log L_{bH\alpha} \gtrsim 43$ or $\log L_{bol} \gtrsim 45$), the T1 distribution is distinct

from the type 2 distribution in the [S II]-panel, and is offset in the [N II]-panel to lower values. Also, the fraction of AGN which reside below the Ke01 line decreases with increasing $L_{bH\alpha}$.

The fraction of poorly-constrained objects increases with $L_{bH\alpha}$ (Fig. 1), due to the decrease in the relative strengths of the narrow lines (Paper II and Fig. 1). Therefore, one may wonder whether this trend with luminosity is not simply due to the limitations of the deblending algorithm. In appendix A we verify the observed trend using high quality mean spectra.

Figure 4 shows the BPT positions of the T1 objects, now subdivided by L/L_{Edd} (derived from $L_{bH\alpha}$ and Δv , using eq. 3 in Paper I). Several trends in the BPT position are apparent. With increasing L/L_{Edd} , an increasing fraction of T1s have high $[O III]/H\beta$, low $[N II]/H\alpha$, and low $[S II]/H\alpha$, as found with increasing $L_{bH\alpha}$ in Fig. 3. The decrease in $[O I]/H\alpha$ with L/L_{Edd} is more pronounced than in Fig. 3: the $[O I]/H\alpha$ span mainly $0.1 - 0.3$ at low L/L_{Edd} , compared to $0.03 - 0.1$ at high L/L_{Edd} . The fraction of LINERs in the BPT-[O I] panel strongly decreases with increasing L/L_{Edd} , from 29% at $\log L/L_{Edd} = -2.5$, to 6% at $\log L/L_{Edd} = -1.8$ and 3% at $\log L/L_{Edd} = -1.2$ and -0.6 .

Figure 5 is similar to Figs. 3 and 4, with different rows designating different bins in L_{AGN}/L_* , measured at the SDSS- z band (see §2.3.1). We note the division of objects between the two high L_{AGN}/L_* bins is not robust in objects with $L_{AGN}/L_* > 1$, due to the possible error in the determination of L_* . The 24 objects with a negative implied L_* appear in the $L_{AGN}/L_* \geq 2$ bin. With increasing L_{AGN}/L_* , $[N II]/H\alpha$ and $[S II]/H\alpha$ decrease, as found with increasing $L_{bH\alpha}$ in Fig. 3, and with increasing L/L_{Edd} in Fig. 4. The T1 sample overlaps the type 2 sample in host dominated objects, and is distinct from the type 2 distribution in AGN dominated objects. Also, the composite fraction decreases from 22% at $L_{AGN}/L_* = 0.04$ to 6% at $L_{AGN}/L_* \geq 2$.

To satisfy the curious reader, the mass dependencies are explored in Appendix B, where we plot the BPT positions of the T1 objects, subdivided by M_{BH} and M_* .

4.2 Comparison with previous type 1 samples

Some earlier studies have measured the BPT positions of smaller samples of type 1 AGN. Dietrich et al. (2005), compiled the BPT positions of earlier Seyfert 1 galaxies in the literature (Cohen 1983, Ho97), and found that Seyfert 1s largely overlap Seyfert 2s (Fig. 7 there). This result is consistent with our finding (Fig. 3, upper panel), that type 1 AGN at low luminosity overlap the positions of type 2 AGN.

Greene & Ho (2007) inspected the narrow line ratio of 229 SDSS type 1 AGN, selected based on the detection of a broad $H\alpha$, similar to T1, but required to have $M_{BH} < 2 \times 10^6 M_\odot$. In their sample, 39% of the objects are classified as Composites or SFs in the BPT-[N II] panel, versus only 20% (Fig. 2) in our sample. However, when we restrict the T1 sample to $M_{BH} < 2 \times 10^6 M_\odot$ (Fig. B1, upper panel), the fraction increases to 36%, consistent with the Greene & Ho (2007) result. In a followup paper (Xiao et al. 2012), they compared the narrow line ratios based on the SDSS spectra with ratios based on spectra from a smaller aperture. The fraction of Composites / SFs decreased to 18%, indicating that extended emission from SF in the host galaxy shifts the BPT position into the composite region at low M_{BH} . Below, we provide further evidence that this effect applies also to composites at higher M_{BH} .

Another prominent feature in the Greene & Ho low M_{BH} sample are objects with high $[O III]/H\beta$, low $[S II]/H\alpha$ and low $[N II]/H\alpha$. Of their type 1's with $[O III]/H\beta > 5$, 10% have

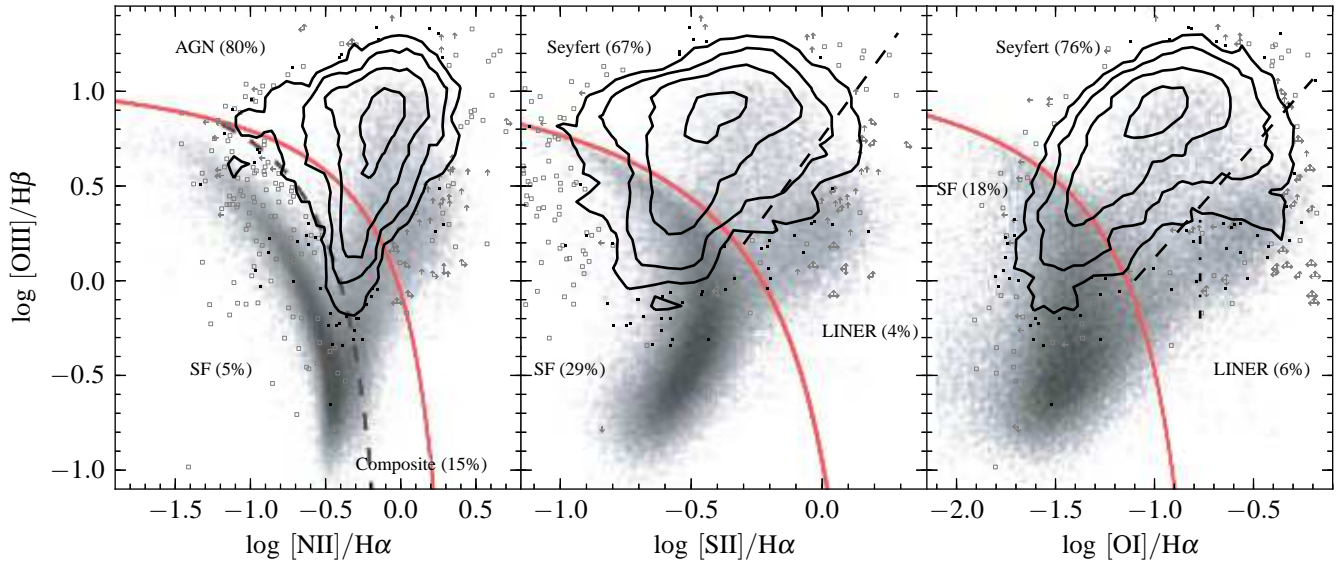


Figure 2. The BPT positions of the 3 175 T1 AGN (solid contours), compared to the narrow line SDSS galaxies (background gray pixels, Fig. 1 in Ke06). Red solid lines are the Ke01 extreme starburst lines, while the dashed lines mark the separation between ‘SF’ and ‘Composites’ in the [N II] panel (Ka03), and between ‘Seyferts’ and ‘LINERs’ in the [S II] and [O I] panels (Ke06). The dash-dotted line in the [O I] panel further divides the LINER group into bona-fide LINERs and ‘transition’ objects (Ho97). The contours encircle regions with 10, 25, 60 and 150 T1 objects per $0.2 \times 0.2 \text{ dex}^2$ bin, respectively. Beyond the outer contour, T1 AGN are marked as in Fig. 1, with upper / lower limits on either of the emission lines denoted by an appropriate arrow. In the [N II] panel, 20% of the T1 objects are below the Ke01 line, and would not be defined as AGN. Of these, 15% are defined as Composites, and 5% as SF galaxies. In the [O I] panel, 190 objects in the sample are LINER 1s, of which 94% (179/190) appear to the right of the Ho97 line. Note that the T1 extends to higher [O III]/H β , and lower [N II]/H α and [S II]/H α , compared to the narrow line galaxies and AGN.

[N II]/H α < 0.3, as found for the entire T1 sample above. These narrow line ratios are also observed in low M_{BH} type 2 samples (Barth et al. 2008), but are clearly missing from type 2s at higher luminosity (Fig. 2). It therefore seems that type 1 and type 2s have similar ratios at low M_{BH} , but become distinct at higher M_{BH} . We examine the reason for this difference below.

Winter et al. (2010) published the BPT positions of a hard X-ray selected AGN sample, of which they identified 33 objects as broad line AGN⁵. Their mean $\log L_{[\text{O III}]}$ is a factor of three higher than the mean in the T1 sample. Five of their type 1s have [S II]/H α < 0.1, and two have [N II]/H α < 0.1, which are not seen in their type 2 sample. These ratios are seen in the T1 sample, but not in the SDSS narrow line sample.

Buttiglione et al. (2010) measured the BPT positions of a radio selected AGN sample. They show a clear trend of decreasing [N II]/H α and [S II]/H α , and increasing [O III]/H β , with increasing [O III] luminosity (Fig. 1 there). Their trend is equivalent to the trend seen in Fig. 3 with $L_{\text{bH}\alpha}$. A similar trend can be seen in Fig. 4 of Wang & Wei (2010), who measured the BPT ratios of Seyferts 1.8s and 1.9s with ROSAT detections. They found that objects in which the AGN dominates the continuum are offset to lower [N II]/H α than objects in which the continuum is host dominated, as can be seen here in Fig. 5.

5 THE NATURE OF T1 AGN WITH LOW [N II]/H α AND LOW [S II]/H α

Figs. 2–5 show that the distributions of the narrow line ratios of the T1 objects extend to values which are not seen in the SDSS narrow line sample, in particular at high L_{bol} , high L/L_{Edd} , and high L_{AGN}/L_* . These non overlapping objects have [O III]/H β similar to type 2s, but lower [N II]/H α and [S II]/H α . In Appendix A we show the offset ratios are not an NLR/BLR deblending artifact. Why are these ratios absent from type 2 samples? what is the physical mechanism that produces them?

5.1 The difference between the T1 and T2 samples

A difference between type 1 and type 2 AGN can be either a failure of the unified model, an orientation-related effect, or simply due to different selection criteria used for creating the two samples. Here, we compare the T1 and T2 (§2.4) samples, and show that selection effects are behind the differences observed in Figs. 2–5. To avoid significant NLR contamination by star formation in the host, which decreases the narrow line ratios to the Composite and SF regions of the BPT plots, we only use the 1 691 T1s and 4 042 T2s with [O III]/H β > 5. This selection criterion is independent of the offset quantities – [N II]/H α and [S II]/H α . A comparison of the Composites and SFs is made in §7 below.

A major difference in the T1 versus T2 selection criteria, is that the T1 sample includes also point sources, and is not selected purely from extended objects. Thus, the T1 sample can extend to L_{AGN}/L_* values larger than possible in the T2 sample. Another related systematic difference is the distribution of M_* values, as the T2 objects are selected by L_* , while in the T1 point sources L_* can be arbitrarily small. The distribution of L_* values is interesting as M_* was found to correlate with the [N II]/H α ratio, via the $M_* - Z$

⁵ They excluded Sy1.8s and Sy1.9s, which selects against low luminosity type 1 AGN (Paper II).

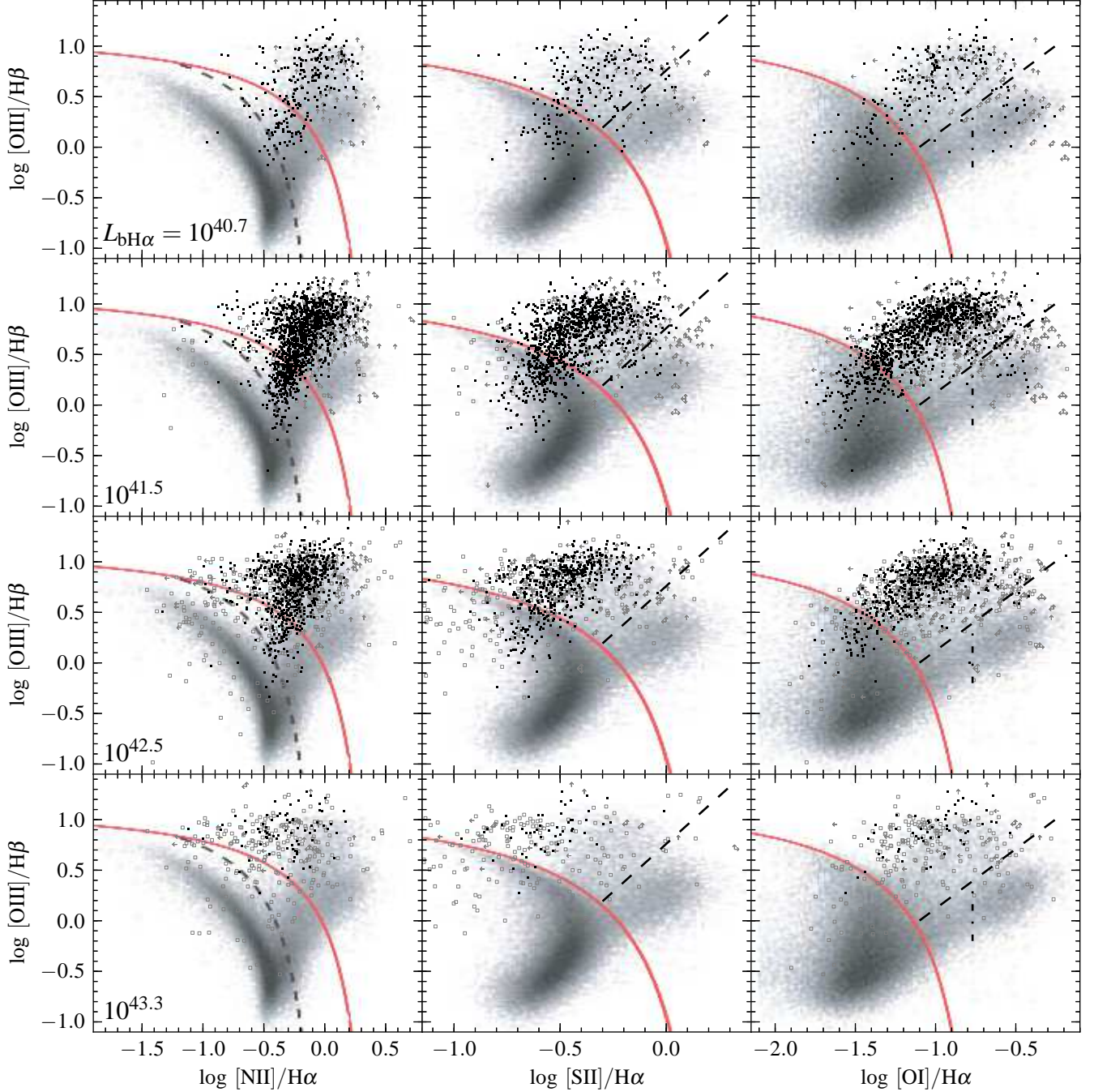


Figure 3. The dependence of the BPT position on the AGN luminosity. The T1 sample markers are as in Fig. 1. The narrow line background and dividing lines are described in Fig. 2. Each row presents T1 AGN from a given decade-wide bin in $L_{\text{bH}\alpha}$. The mean $L_{\text{bH}\alpha}$ in each bin are noted (in erg s^{-1}). At $\log L_{\text{bH}\alpha} = 40.7$ ($L_{\text{bol}} = 42.8$), T1 AGN overlap the narrow line sample. With increasing luminosity, the mean $[\text{N II}]/\text{H}\alpha$ and $[\text{S II}]/\text{H}\alpha$ decrease. At quasar luminosities ($\log L_{\text{bH}\alpha} \gtrsim 43$ or $\log L_{\text{bol}} \gtrsim 45$), a large fraction of the T1 AGN occupy a region in the $[\text{N II}]$ and $[\text{S II}]$ panels which is distinct from the type 2 distribution.

relation of galaxies, and the dependence of $[\text{N II}]/\text{H}\alpha$ on Z (Groves et al. 2006, see below).

In Figure 6, we therefore plot contours of the distribution of T1s and T2s in the M_* vs. L_{AGN}/L_* plane. The T1 sample is divided according to the two SDSS surveys from which it is derived, those selected from the SDSS galaxy survey, and the point-sources from the SDSS quasar survey. We note that at $L_{\text{AGN}}/L_* > 1$, L_* (and M_*) can be significantly overestimated (§2.3.1), therefore the true

L_{AGN}/L_* may be higher and the true M_* may be lower than plotted. In the 17% of T1 point sources with $L_{\text{AGN}}/L_* > 3$, L_* is not well-constrained either from below or from above, therefore we abruptly cut the distribution. This cut does not affect the conclusions below. In the T2 sample, L_{AGN} is derived from $L_{[\text{O III}]}$ (Paper II), and L_* and M_* are derived from the observed SDSS z -band luminosity, using the same M/L as in T1s.

The T2s are all selected from the SDSS galaxy survey. The

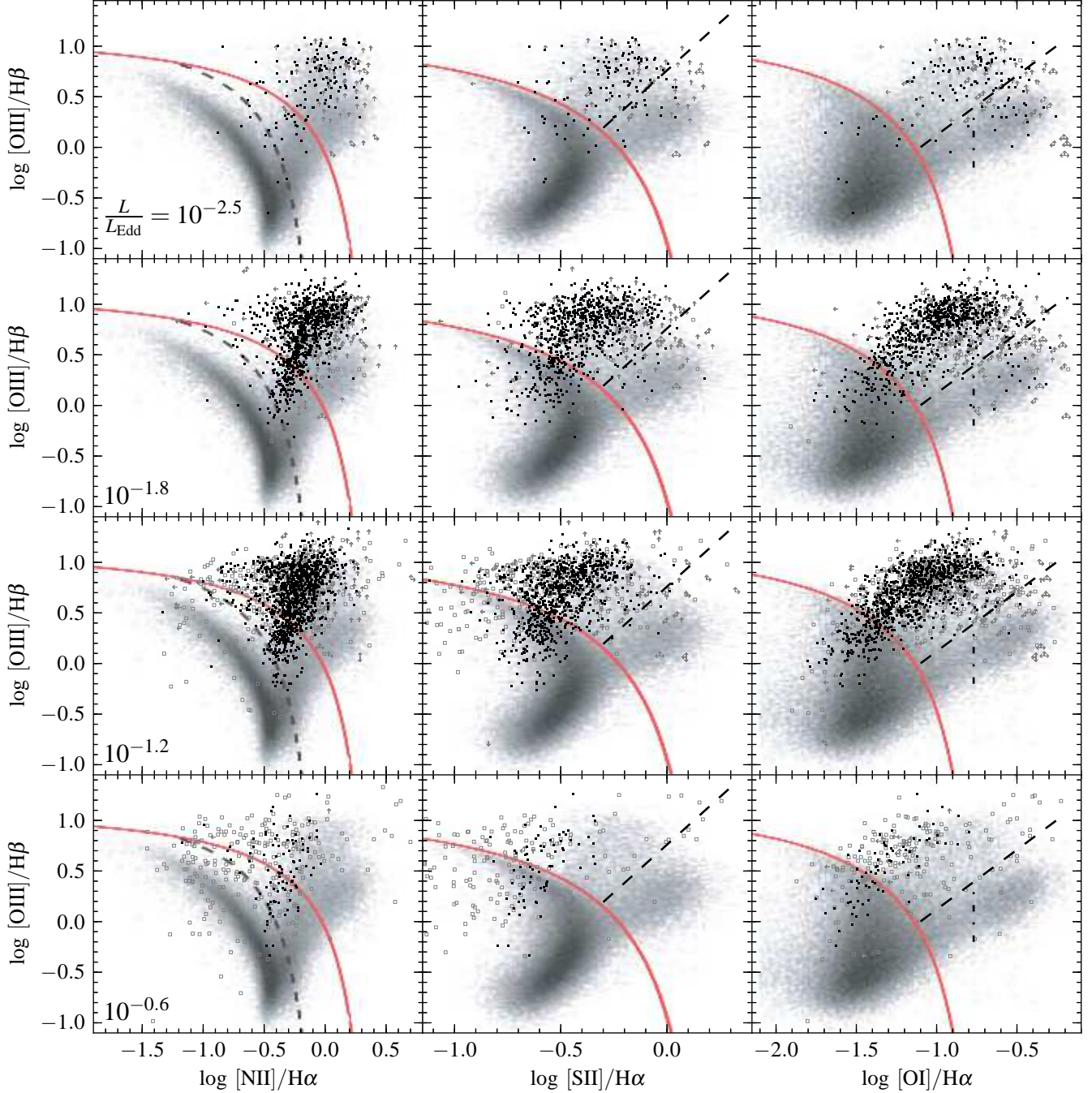


Figure 4. As Fig. 3, for the dependence of the BPT position on L/L_{Edd} . Each row presents T1 AGN for a given L/L_{Edd} bin (0.75 dex wide). The mean L/L_{Edd} in each bin is noted in the lower left corners. With increasing L/L_{Edd} , the T1 AGN move to the left in all BPT panels. Also, at $\log L/L_{\text{Edd}} = -2.5$, 29% of the T1 sample are in the LINER region of the [O I] panel, compared to 6% in the entire T1 sample.

distribution of the T1s from the same survey overlaps well the distribution of T2s. The T1 point sources however are clearly offset to higher L_{AGN}/L_* , and constitute an AGN population which does not appear in the T2 sample. As Fig. 5 shows, the T1s become offset from T2s at the higher L_{AGN}/L_* values. Thus, the apparent differences between the T1 and T2 BPT positions reflects their different L_{AGN}/L_* values, which controls the BPT positions. Figure 7 explores this effect more quantitatively. The T1s and T2s are binned by the $[\text{N II}]/\text{H}\alpha$ values, and the distributions of the different bins in the M_* vs. L_{AGN}/L_* plane is presented.

In the T1 sample, M_* decreases and L_{AGN}/L_* increases with decreasing $[\text{N II}]/\text{H}\alpha$. The T2 sample shows a similar trend, but it does not extend to the high L_{AGN}/L_* occupied by objects with $[\text{N II}]/\text{H}\alpha < 0.2$. In fact, already T2s with $[\text{N II}]/\text{H}\alpha < 0.6$ are rare, constituting only 8% of the T2 sample, compared to the 39% of T1s that have $[\text{N II}]/\text{H}\alpha < 0.6$. Therefore, the T2 objects do not extend to the low $[\text{N II}]/\text{H}\alpha$ values, seen in the T1 sample, as these values occur at high L_{AGN}/L_* values, which the T2 objects cannot have by their selection.

A similar analysis using the $[\text{S II}]/\text{H}\alpha$ values, instead of

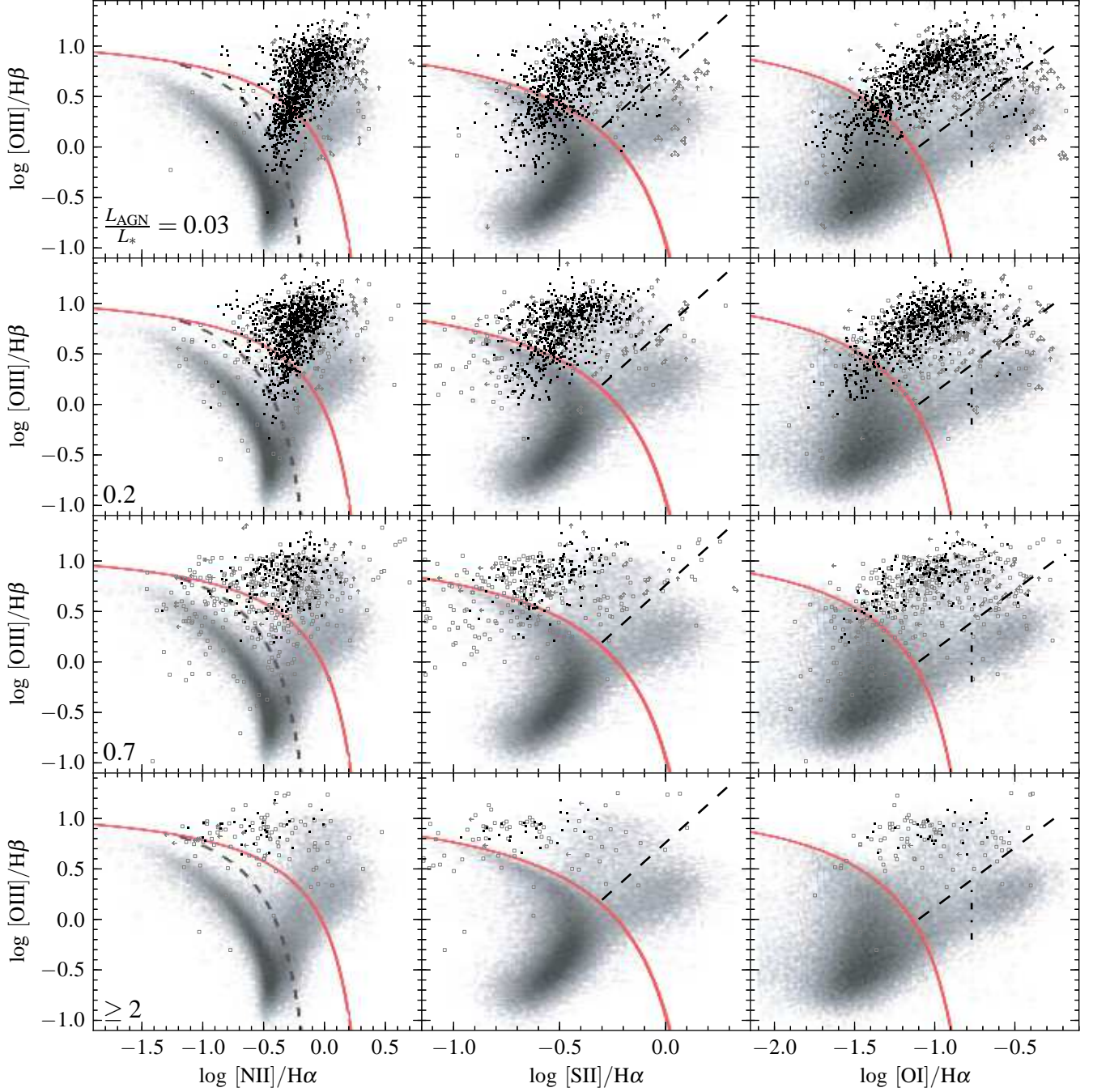


Figure 5. As Fig. 3, for the dependence of the BPT position on L_{AGN}/L_* . Each row presents T1 AGN from a given L_{AGN}/L_* bin (0.7 dex wide). The L_{AGN}/L_* is calculated at the SDSS z -band, and the mean values are noted in the lower left corners. The T1 AGN move to lower $[\text{N II}]/\text{H}\alpha$ and $[\text{S II}]/\text{H}\alpha$ with increasing L_{AGN}/L_* , similar to the trend with $L_{\text{BH}\alpha}$ seen in Fig. 3. The composite fraction decreases from 22% at $L_{\text{AGN}}/L_* = 0.03$ to 6% at $L_{\text{AGN}}/L_* \geq 2$.

$[\text{N II}]/\text{H}\alpha$, demonstrates that the low $[\text{S II}]/\text{H}\alpha$ values seen in the T1 sample at high L_{AGN}/L_* (Fig. 5) are absent from the T2 sample for the same reason.

5.2 The quantitative change in $[\text{N II}]/\text{H}\alpha$ and $[\text{S II}]/\text{H}\alpha$

After addressing why the low $[\text{N II}]/\text{H}\alpha$ and $[\text{S II}]/\text{H}\alpha$ ratios seen in the T1 sample are absent from the T2 sample, we now quantify

the dependence of $[\text{N II}]/\text{H}\alpha$ and $[\text{S II}]/\text{H}\alpha$ on the observed AGN and host properties.

As can be seen in Figs. 3, 5 and 7, $[\text{N II}]/\text{H}\alpha$ decreases both with increasing L_{AGN} and with decreasing L_* . Below we explore the two effects independently. We bin the T1 objects with $[\text{O III}]/\text{H}\beta > 5$ (to avoid host contamination) based on M_* and L_{bol} ($\equiv 130 \times L_{\text{BH}\alpha}$) in the following manner. The objects are sorted by L_{bol} and divided into four equal size groups. Each of these groups is then sorted by M_* , and again divided into four equal size groups. This ensures similar statistical errors in all bins. We disre-

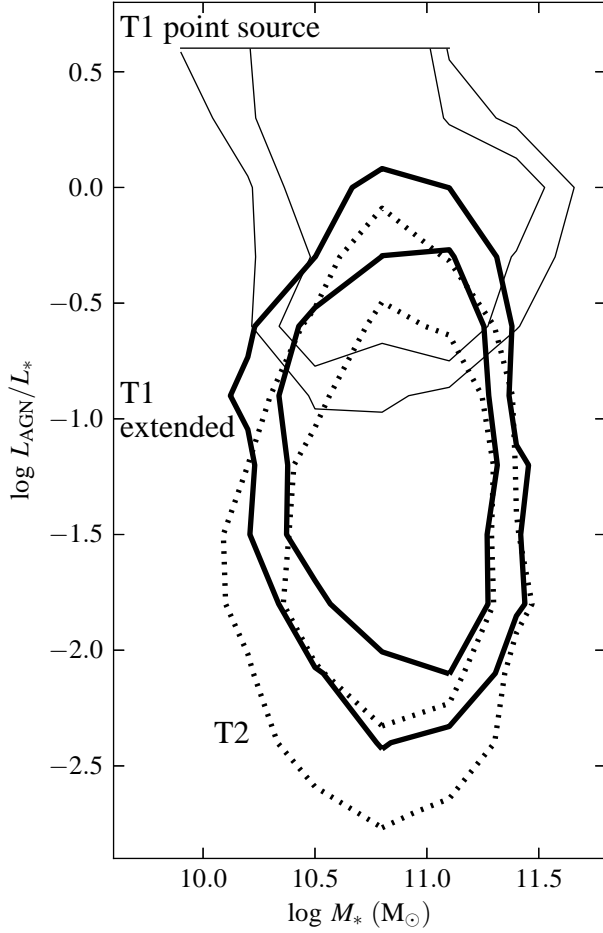


Figure 6. The distribution of the T1 and T2 AGN, with $[\text{O III}]/\text{H}\beta > 5$, in the M_* versus L_{AGN}/L_* plane. The distributions are denoted by two contour lines, which indicate the number of objects per $0.3 \times 0.3 \text{ dex}^2$, 1% of the size of the group for the outer contour, and 2.5% for the inner contour. The three groups marked are T1 selected as point sources (thin solid), T1 selected to have extended morphology (thick solid), and T2s which are all selected to have an extended morphology (dotted). At $L_{\text{AGN}}/L_* > 1$, L_* (and M_*) may be overestimated (§2.3.1). In the 17% of T1 point sources with $L_{\text{AGN}}/L_* > 3$, L_* is not well-constrained either from below or from above, therefore we abruptly cut the distribution. The extended T1 distribution overlaps the T2 distribution, as expected from their common selection criteria (and AGN unification). The T1 point sources, selected by their non-stellar colors, are offset to higher L_{AGN}/L_* than AGN with an extended morphology, and constitute an AGN population which does not appear in the T2 sample.

gard the 12% of the objects with $L_{\text{AGN}}/L_* > 1$, in which the M_* measured has a large error (§2.3.1).

Figure 8 presents the derived relations of the mean values of $[\text{N II}]/\text{H}\alpha$, $[\text{S II}]/\text{H}\alpha$, $[\text{N II}]/[\text{S II}]$, and $L_{\text{nH}\alpha}/L_{\text{bH}\alpha}$ as a function of M_* , for different L_{bol} . Error bars denote the error in the mean. The upper panel shows that the mean $[\text{N II}]/\text{H}\alpha$ increases with M_* at a fixed L_{bol} , an increase of $\sim 0.3 \text{ dex}$ over $\sim 0.7 \text{ dex}$ in M_* . Also, the mean $[\text{N II}]/\text{H}\alpha$ decreases with L_{bol} , at a fixed M_* , a decrease of $\sim 0.3 \text{ dex}$ over $\sim 1.7 \text{ decades}$ in L_{bol} . The second panel shows that $[\text{S II}]/\text{H}\alpha$ increases only slightly with M_* at a fixed L_{bol} . However, the mean $[\text{S II}]/\text{H}\alpha$ decreases with L_{bol} at a fixed M_* , similar to the decrease in $[\text{N II}]/\text{H}\alpha$ with L_{bol} in the upper panel. The rela-

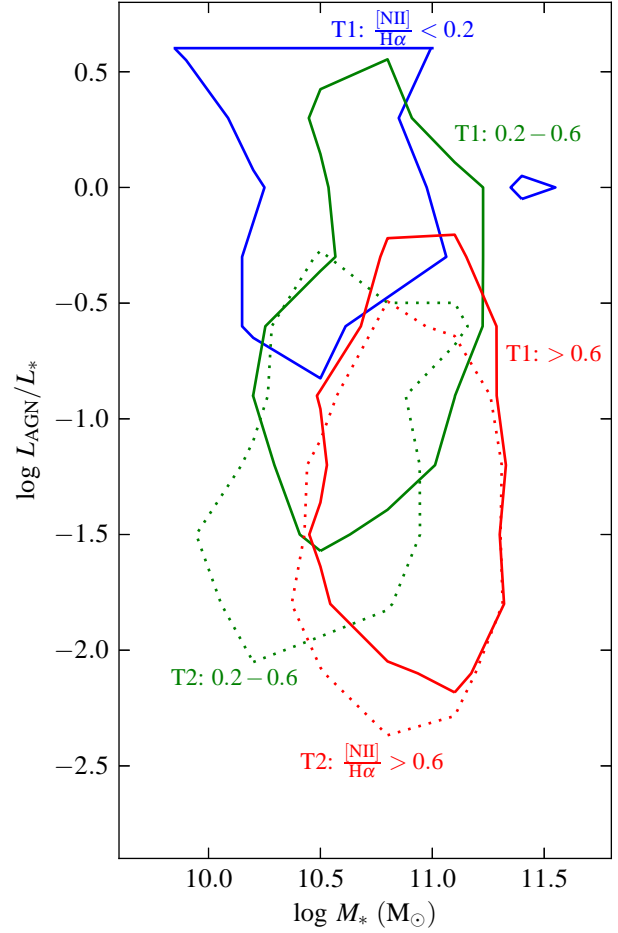


Figure 7. The distribution of T1 and T2 AGN samples with $[\text{O III}]/\text{H}\beta > 5$ in the M_* versus L_{AGN}/L_* plane. Each sample is grouped into bins in $[\text{N II}]/\text{H}\alpha$. The contour line of each bin is equivalent to the inner contour of each group in Fig. 6. The $[\text{N II}]/\text{H}\alpha$ range of each bin is noted near the contour, and coded by color. T1 contours are solid, and T2 contours are dotted. In the T1 sample, the distribution moves to lower M_* and higher L_{AGN}/L_* with decreasing $[\text{N II}]/\text{H}\alpha$. T2s follow a similar trend, but they do not extend to the high L_{AGN}/L_* occupied by objects with $[\text{N II}]/\text{H}\alpha < 0.2$ (Fig. 6). Thus, the absence of $[\text{N II}]/\text{H}\alpha < 0.2$ AGN from the T2 sample just reflects its selection against high L_{AGN}/L_* objects, which are observed to have a low $[\text{N II}]/\text{H}\alpha < 0.2$.

tive trends of $[\text{N II}]$ and $[\text{S II}]$ are most apparent in the third panel. Clearly, $[\text{N II}]/[\text{S II}]$ strongly increases with M_* , and is almost independent of L_{bol} , with only a small decrease at the highest L_{bol} bin, at low M_* .

What are the physical mechanisms behind these trends in $[\text{N II}]/\text{H}\alpha$ and $[\text{S II}]/\text{H}\alpha$? The similarity of the behavior of $[\text{N II}]/\text{H}\alpha$ and $[\text{S II}]/\text{H}\alpha$ vs. L_{bol} , in contrast to the different behavior vs. M_* , suggests there are two distinct mechanisms at play. We address them separately below.

5.3 The trend with M_*

5.3.1 M_* vs. Z_{NLR}

An increase of $[\text{N II}]/\text{H}\alpha$ with M_* has been observed in type 2 AGN by Groves et al. (2006), qualitatively similar to the trend we see

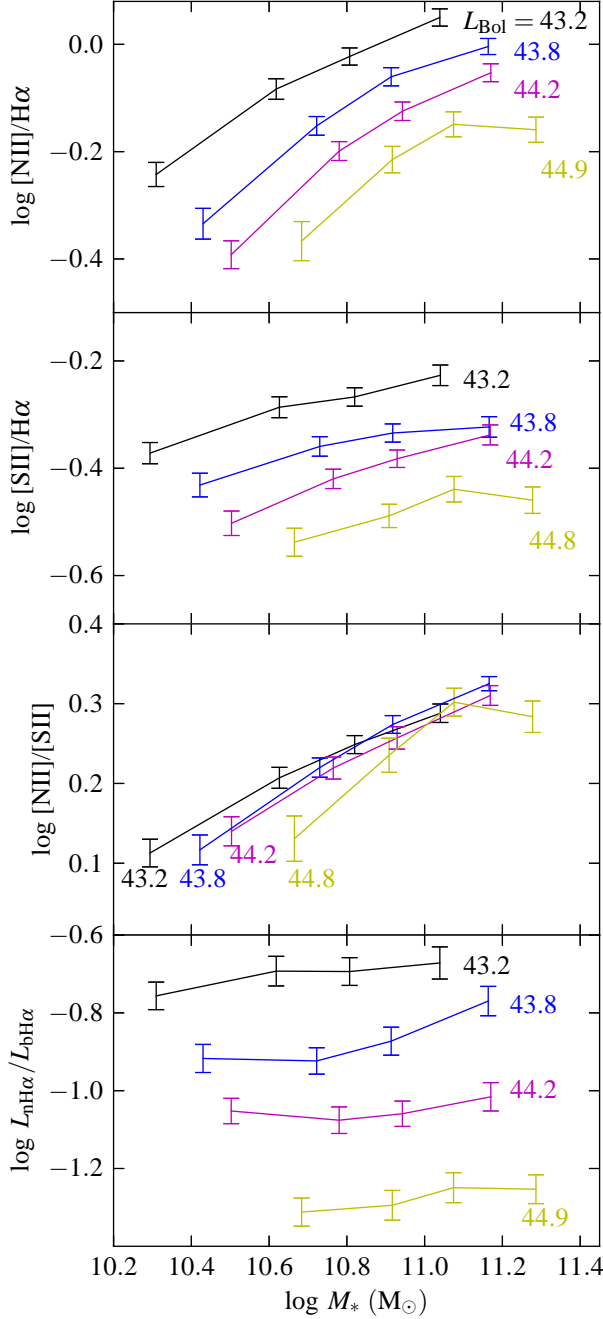


Figure 8. The dependence of the mean line ratios of the T1 objects (with $[\text{O III}]/\text{H}\beta > 5$) on L_{bol} and M_* . Given L_{bol} bins are connected by solid lines (mean $\log L_{\text{bol}}$ noted). Error bars denote the uncertainty in the mean value. Each of the 16 bins in the top and bottom panels has 92 objects, while each bin in the middle panels has 76 objects. **Top panel** The mean $[\text{N II}]/\text{H}\alpha$ increases with M_* at a fixed L_{bol} , and decreases with increasing L_{bol} at a fixed M_* . **Second panel** The mean $[\text{S II}]/\text{H}\alpha$ decreases with increasing L_{bol} at a fixed M_* . At a fixed L_{bol} , $[\text{S II}]/\text{H}\alpha$ only slightly increases with M_* . **Third panel** The mean $[\text{N II}]/[\text{S II}]$ is determined by M_* and is almost independent of L_{bol} . The three trends with M_* shown above likely reflect an increase of Z_{NLR} with M_* . **Bottom panel** The mean $L_{\text{nH}\alpha}/L_{\text{bH}\alpha}$ decreases with L_{bol} and is largely independent of M_* . The $L_{\text{nH}\alpha}/L_{\text{bH}\alpha}$ is a measure of the NLR covering factor (Paper II). Therefore, the decrease in $[\text{N II}]/\text{H}\alpha$ and $[\text{S II}]/\text{H}\alpha$ with L_{bol} , at a fix M_* , is likely related to the decrease in NLR covering factor with increasing L_{bol} .

in T1 AGN (Fig. 8). As mentioned above, Groves et al. claimed this trend originates from the $M_* - Z$ relation found in quiescent galaxies.

A dependence of $[\text{N II}]/\text{H}\alpha$ on Z_{NLR} is expected since Nitrogen is a secondary nucleosynthesis product, and hence its abundance increases as Z^2 for $Z > 0.5 Z_\odot$ (e.g. van Zee et al. 1998). This secondary nature also implies that the relative abundances of N and S in the NLR increases $\propto Z_{\text{NLR}}$. Fig. 8 shows clearly that the $[\text{N II}]/[\text{S II}]$ increases with M_* , consistent with a change in Z_{NLR} with M_* .

In the photoionization models of Groves et al. (2004, Fig. 19 there), $[\text{N II}]/\text{H}\alpha$ increases roughly like $Z_{\text{NLR}}^{1.5}$, compared to $[\text{S II}]/\text{H}\alpha$ which increases roughly like $Z_{\text{NLR}}^{0.5}$, supporting $[\text{N II}]/[\text{S II}] \propto (\text{N/S})_{\text{NLR}} \propto Z_{\text{NLR}}$. Hence, the $[\text{N II}]/[\text{S II}]$ panel of Fig. 8 implies a change of 0.2 dex in Z_{NLR} over 0.8 dex in M_* . For comparison, Groves et al. (2006) find a change of 0.2–0.3 dex in Z_{NLR} over two decades in M_* . We speculate that our steeper $M_* - Z_{\text{NLR}}$ relation is because that by using $[\text{N II}]/[\text{S II}]$, we factored out the decrease of $[\text{N II}]/\text{H}\alpha$ with L_{bol} (upper panel in Fig. 8), which flattens the relation found by Groves et al.

In inactive galaxies, Tremonti et al. (2004) found an increase of ~ 0.1 dex in the mean gas phase Z at $10.4 < \log M_* < 11.2$, half the increase of 0.2 dex in Z_{NLR} estimated here.

5.3.2 Z_{NLR} vs. Z_{BLR}

Are there any additional differences in the spectra of objects with high and low $[\text{N II}]/\text{H}\alpha$? Figure 9 compares the mean spectra of objects with $[\text{N II}]/\text{H}\alpha < 0.2$ and objects with $[\text{N II}]/\text{H}\alpha > 0.6$. To avoid other known trends, and isolate only $[\text{N II}]/\text{H}\alpha$ related trends, we match each of the T1s with $[\text{N II}]/\text{H}\alpha < 0.2$ with a T1 that has $[\text{N II}]/\text{H}\alpha > 0.6$ with the same L_{bol} up to 0.1 dex, and the same Δv up to 0.05 dex. Matching by L_{bol} ensures we are freezing the L_{bol} -related effect seen in Fig. 8, while matching also by Δv indicates we are freezing also M_{BH} (via eq. 2 in Paper I) and L/L_{Edd} and the host of spectral properties related to it (e.g. Boroson & Green 1992). Of the 98 T1s with $[\text{N II}]/\text{H}\alpha < 0.2$, 79 have such matches.

The mean spectra of the two groups of objects are calculated by geometrically averaging luminosity densities of spectrum pixels with the same restframe wavelength λ , rounded to 10^{-4} in $\log \lambda$. The bottom spectrum is the difference between the two composite spectra, and the insets zoom in on the areas delimited by the dashed lines. The most striking feature of the residual is the strong BLR Fe II multiplets at $\sim 4600\text{\AA}$ and $\sim 5300\text{\AA}$.

The luminosity of the optical Fe II multiplets is expected to increase with iron column density, and therefore with Z_{BLR} , to a power of 0.8–0.9 (Verner et al. 2003, Baldwin et al. 2004, Shields et al. 2010). Thus, Fig. 9 provides interesting evidence that the BLR metallicity, Z_{BLR} , is related to Z_{NLR} . There is a well-known relation between the Fe II equivalent width and L/L_{Edd} (Boroson & Green 1992), but since the two composites are matched in L/L_{Edd} , this effect should not be present.

Shields et al. (2010) found that when binning by $L(\text{Fe II})/L_{\text{bH}\beta}$, $[\text{N II}]/[\text{S II}]$ increases by a factor of two for an increase of a factor of ten in $L(\text{Fe II})/L_{\text{bH}\beta}$. They concluded that the Fe II strength increases with Z_{NLR} , but the dispersion in Fe II is not dominated by Z_{NLR} . In Fig. 9, the composite spectra differ by a factor of ~ 3 in $[\text{N II}]/[\text{S II}]$, and a factor ~ 2 in $L(\text{Fe II})$, suggesting that for a constant L/L_{Edd} , Z_{NLR} and Z_{BLR} change in unison.

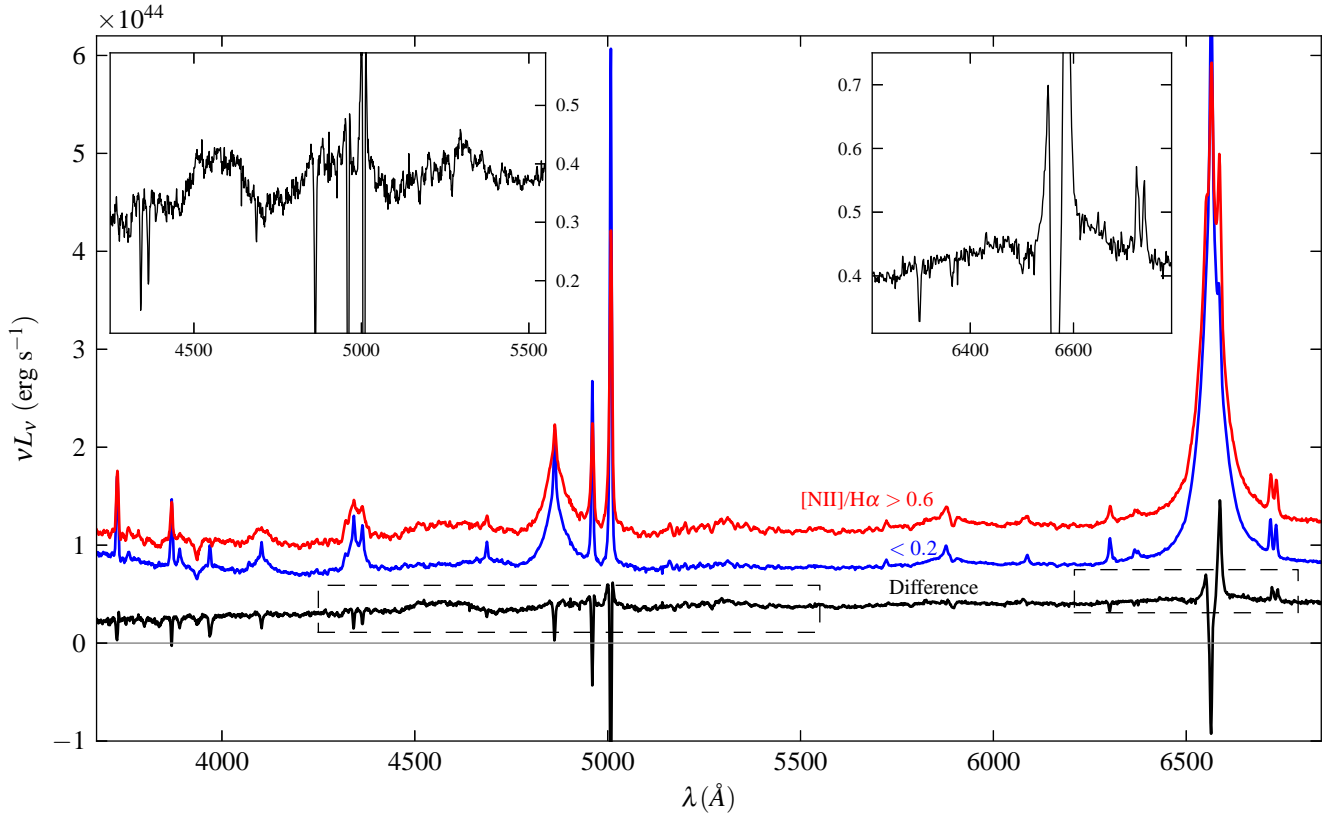


Figure 9. The difference between mean spectra of T1 AGN with high (> 0.6) and low (< 0.2) $[\text{N II}]/\text{H}\alpha$ values. The two samples are selected to match in $L_{\text{bH}\alpha}$ and Δv , and thus in L/L_{Edd} as well. Insets zoom in on the dashed rectangles in the difference spectrum. The high $[\text{N II}]/\text{H}\alpha$ spectrum also has stronger BLR Fe II multiplets at $\sim 4600\text{\AA}$ and $\sim 5300\text{\AA}$, which are expected to increase with Z_{BLR} . Therefore, at a fixed L_{bol} and L/L_{Edd} , Z_{NLR} and Z_{BLR} appear to be related. The high $[\text{N II}]/\text{H}\alpha$ spectrum also shows a larger M_* , evident from the red slope and the stellar absorption features at 3934\AA and 6500\AA in the residual. Thus, Z_{BLR} also appears to be at least partly driven by the host M_* .

The mean $\log M_*$ of the low and high $[\text{N II}]/\text{H}\alpha$ composite spectra are 10.5 and 10.9, respectively. This difference in M_* can be seen in the residual spectrum, which has a red optical slope, a $[\text{Ca II}] \text{K } \lambda 3934$ absorption feature, and a stellar absorption blend at 6500\AA . The two groups are selected to have the same mean M_{BH} , and should thus have similar mean bulge mass (Magorrian et al 1998). The different measured mean M_* values of the two groups should therefore reflect differences in the mean disk masses, where the higher metallicity group has a higher disk/bulge mass ratio.

Hamann & Ferland (1993, 1999) found that in quasars, Z_{BLR} (derived from the NV / CIV ratio) increases with L_{bol} . They speculated that the increase in Z_{BLR} with L_{bol} is probably due to the increase of Z_{BLR} with M_* , and the strong relation between M_* and L_{bol} in the quasar samples they used. Here, we confirm their claim by showing Z_{BLR} increases with M_* directly. At a given M_* , the mean $[\text{N II}]/[\text{S II}]$ remains constant with L_{bol} (Fig. 8), and only slightly decreases at the highest L_{bol} . Furthermore, this slight decrease could be due to improper deblending of the $[\text{N II}]$ profile from the broad $\text{H}\alpha$ profile at high $L_{\text{bH}\alpha}$ (see Fig. 1). Therefore, we find no evidence for a direct $Z - L_{\text{bol}}$ trend.

5.4 The trend with L_{bol}

As mentioned above, the decrease of $[\text{N II}]/\text{H}\alpha$ with L_{bol} is probably not a Z_{NLR} effect. Therefore, deriving Z_{NLR} in quasars from

$[\text{N II}]/\text{H}\alpha$, using the calibration of lower luminosity AGN (e.g. Husemann et al. 2011), will underestimate Z_{NLR} .

A hint on the physical source of the trend with L_{bol} can be seen in the bottom panel of Fig. 8. The $L_{\text{nH}\alpha}/L_{\text{bH}\alpha}$ decreases with L_{bol} , as found in Paper II, but is only weakly dependent of M_* , if at all. Therefore, it seems that the decrease in $[\text{N II}]/\text{H}\alpha$ and $[\text{S II}]/\text{H}\alpha$ with L_{bol} , at a given M_* , is related to the decrease in $L_{\text{nH}\alpha}/L_{\text{bH}\alpha}$. In Paper II, we presented evidence that the $L_{\text{nH}\alpha}/L_{\text{bH}\alpha}$ vs. L_{bol} trend is due to a decrease in the NLR covering factor with L_{bol} . The physical connection between the decrease in $[\text{S II}]/\text{H}\alpha$ and $[\text{N II}]/\text{H}\alpha$ and the decrease in NLR covering factor remains an open question.

6 LINERS

Ke06 found that at a fixed L/L_{Edd} , the difference between host properties of Seyferts and LINERs disappear. Their conclusion was that the observed difference in host properties between Seyferts and LINERs is only a secondary effect, which results from their difference in L/L_{Edd} (Ho 2002, Ke06). Here, we show that the observed large difference between Seyferts and LINERs in terms of the fraction which shows broad lines (Ho et al. 1997b, Ho 2008), is also a secondary effect of their difference in L/L_{Edd} , and at a fixed L/L_{Edd} the difference disappears.

Following Ke06, we create subsamples of the T1 and T2 samples which include objects classified as AGN in the BPT- $[\text{N II}]$

panel, and as either Seyferts or LINERs in the BPT-[S II] and BPT-[O I] panels (Fig. 2). We use only objects with consistent BPT-[S II] and BPT-[O I] classifications. We use the bulge stellar dispersion σ_* to derive M_{BH} in T2s (Gülekci et al. 2009). We disregard the 8% of the T2s with surface mass density $< 3 \times 10^8 \text{ M}_\odot \text{ kpc}^{-2}$, in which the σ_* measured by the SDSS may be overestimated due to disk light contamination (Kauffmann et al. 2003c, Heckman et al. 2004).

Following the above criteria, the T2 subsample includes 4938 Seyfert 2s and 4292 LINER 2s. The T1 subsample includes 1910 Seyfert 1s and 76 LINER 1s. Thus, LINERs constitute 50% of the T2 sample, but only 4% of the T1 sample. Our purpose is to further understand the origin of this large difference.

In 44 objects from the LINER 1 group, the classification is ambiguous, either due to upper/lower limits on the BPT ratios, or because their narrow line ratios are poorly constrained (§2.2.3). We address this uncertainty below. The fraction of Seyfert 1s with an ambiguous classification is negligible.

In the T1 sample, we derive the L/L_{Edd} from $L_{\text{bH}\alpha}$ and Δv , using eq. 3 in Paper I. In the T2 sample, we derive L_{bol} from $L_{[\text{O III}]}$ (Paper II), which was derived from the $L_{[\text{O III}]} - L_{\text{bH}\alpha}$ relation in the T1 sample (eq. 3 there). We note in passing that in LINERs, almost by definition, $L_{[\text{O III}]} / L_{\text{bH}\alpha}$ is expected to be lower (see factor of two drop in $L_{[\text{O III}]} / L_{\text{bH}\alpha}$ in the lower-left panel of Fig. 6 in Paper II), so the true L_{bol} in LINERs is likely a bit higher than our derived L_{bol} .

Figure 10 presents the fraction of LINERs 2 out of the T2 sample, as a function of L/L_{Edd} . Seyfert 2s and LINER 2s are cleanly separated in L/L_{Edd} , as found by Ke06. At $L/L_{\text{Edd}} > -2$ all T2s are Seyferts, while at $\log L/L_{\text{Edd}} < -4$ all T2s are LINERs. Fig. 1 also presents LINER 1 fractions out of the T1 sample, at different L/L_{Edd} . The uncertainty in the LINER 1 fraction is due to the 44 T1 objects with an ambiguous LINER classification. At a fixed L/L_{Edd} , the fraction of LINER 1s is consistent with the fraction of LINER 2s. Therefore, the small fraction of LINERs in the T1 sample results from the fact that the sample does not extend to low enough L/L_{Edd} , where LINERs become the dominant population.

Why do the T1 and T2 samples differ in their L/L_{Edd} distribution? The fact that all T1s have $L/L_{\text{Edd}} > 10^{-3}$ could be a detection limit, since low L/L_{Edd} have weak and wide broad $\text{H}\alpha$ features, which are hard to distinguish from the stellar continuum (see Fig. 6 in Paper I). Alternatively, there may be a physical reason for a lack of low L/L_{Edd} type 1 AGN, related to the subject of ‘true type 2’ AGN (see further discussions in Laor 2003; Laor & Davis 2011).

The fact that the probability an object is a Seyfert or a LINER does not depend on whether the BLR is detected or not, indicates the transition from Seyferts to LINER does not affect the BLR. This may indicate that the physical difference between these two type of objects occurs beyond the BLR, and hence external to the central source. I.e., Seyferts and LINERs may differ by the conditions in the circumnuclear gas, and not by a different accretion mode. Such a scenario implies that the intrinsic UV and X-ray emission of LINERs and Seyferts should not be distinct, as found by Maoz et al. (2005, 2007). Though, these latter results are disputed (see review in Ho 2008).

7 T1 AGN CLASSIFIED AS COMPOSITES AND SF

Why do some of the T1 objects display narrow line ratios characteristic of Composites and SF galaxies? Can such line ratios be powered by accretion onto a massive black hole, or does it result

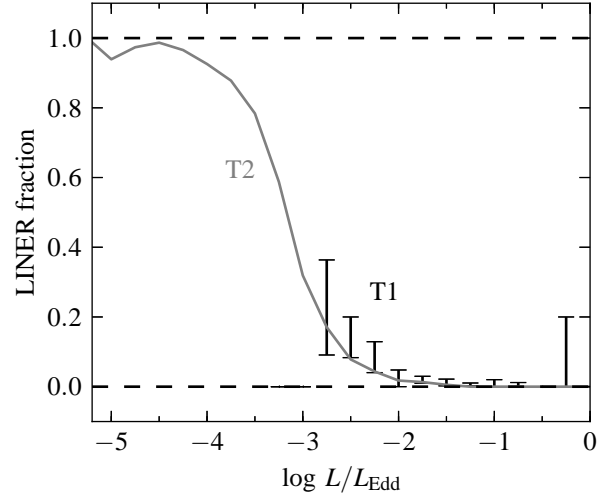


Figure 10. The fraction of LINERs in the T1 and T2 samples, as a function of L/L_{Edd} . The solid gray line indicates the fraction of LINERs in the T2 sample, in 0.25 dec L/L_{Edd} bins, where L/L_{Edd} is derived from $L_{[\text{O III}]}$ and σ_* . The fractions of LINERs in the T1 sample are denoted by error bars, where L/L_{Edd} is derived from $L_{\text{bH}\alpha}$ and Δv . The uncertainty is due to T1 objects with an ambiguous classification. At $\log L/L_{\text{Edd}} > -2$ all T2s are Seyferts, while at $\log L/L_{\text{Edd}} < -4$ all T2s are LINERs. At a fixed L/L_{Edd} , the fraction of LINER 1s is consistent with the fraction of LINER 2s within the uncertainties. The low fraction of LINERs in the T1 sample ($\sim 4\%$) versus the high fraction in the T2 sample ($\sim 50\%$) results from the difference in the L/L_{Edd} distribution of the T1 and T2 samples. The lack of $L/L_{\text{Edd}} < 10^{-3}$ T1s could be due to detection limits, or due to a physical absence of low L/L_{Edd} type 1 AGN.

from host contamination? The fraction of T1s classified as Composites increases with L_*/L_{AGN} at the SDSS- z band (Fig. 5), which suggests a host contamination effect. Below we explore quantitatively the host contamination, based on other indicators, and its relation to the narrow line ratios. We compare the $L_{\text{nH}\alpha}/L_{\text{bH}\alpha}$ and $L_{\text{UV}}/L_{\text{bH}\alpha}$ of Composites with those of T1s which fall above the Ke01 line in the BPT-[N II] panel (hereby called ‘pure-AGN’). In pure-AGN $L_{\text{nH}\alpha}$ and L_{UV} correlate with $L_{\text{bH}\alpha}$, thus host contribution should manifest as higher $L_{\text{nH}\alpha}/L_{\text{bH}\alpha}$ and $L_{\text{UV}}/L_{\text{bH}\alpha}$ due to line and continuum emission from the SF regions.

In Table 4, we list the geometrical mean of $L_{\text{bH}\alpha}$ and $L_{\text{nH}\alpha}/L_{\text{bH}\alpha}$ for the T1 AGN classified as pure-AGN, Composites and SF. The SF group is divided into ‘SF-robust’ (32 objects) and ‘SF-non robust’ (69 objects), depending on whether their narrow line ratios are well-constrained (§2.2.3). This division is to guard against systematic uncertainties in the less secure measurements. As seen in the lower left panel of Fig. 4, non-robust SFs tend to have high L/L_{Edd} , where the NLR is weak and the broad $\text{H}\alpha$ is relatively narrow, making the NLR / BLR deblending difficult. It is therefore possible that in non-robust SFs broad Balmer flux was mistakenly assigned to the narrow Balmer lines, and their SF classification is not real. In the Composite and pure-AGN classes poorly constrained objects are less abundant (17%), and therefore a separate group is not required.

Since the mean AGN $L_{\text{nH}\alpha}/L_{\text{bH}\alpha}$ decreases with increasing AGN luminosity (Paper II), we compare each classification with a pure-AGN matched in $L_{\text{bH}\alpha}$. The matched groups are constructed by randomly selecting 1–4 pure-AGN T1 objects with the same $L_{\text{bH}\alpha}$ (up to 0.1 dex), for each Composite or SF (see Table 4). The geometrical mean $L_{\text{nH}\alpha}/L_{\text{bH}\alpha}$ of the Composites is 0.27, compared

BPT-[N II] Classification	N	$L_{\text{bH}\alpha}$	$L_{\text{nH}\alpha}/L_{\text{bH}\alpha}$	$L_{\text{UV}}/L_{\text{bH}\alpha}$
pure-AGN	2303	42.0	0.11	33
Composites	407	41.8	0.27	54
L matched pure-AGN	407	41.8	0.12	36
SF-robust	32	41.6	$0.44 \pm 20\%$	$62 \pm 20\%$
L matched pure-AGN	128	41.6	$0.14 \pm 10\%$	$40 \pm 10\%$
SF-non robust	69	42.8	$0.16 \pm 10\%$	$37 \pm 10\%$
L matched pure-AGN	207	42.7	$0.06 \pm 10\%$	$29 \pm 10\%$

Table 4. The mean $L_{\text{nH}\alpha}/L_{\text{bH}\alpha}$ and $L_{\text{UV}}/L_{\text{bH}\alpha}$ of different BPT-[N II] classifications. The SF objects are divided according to whether their narrow line measurements are robust (§2.2.3). In the pure-AGN and composite groups, 83% of the objects have robust measurements. The $L_{\text{bH}\alpha}$ (in $\log \text{erg s}^{-1}$), $L_{\text{nH}\alpha}/L_{\text{bH}\alpha}$ and $L_{\text{UV}}/L_{\text{bH}\alpha}$ values are the geometrical means, with the uncertainty in the mean noted only if it is $> 5\%$.

to 0.12 in the matched pure-AGN. Therefore, the $L_{\text{nH}\alpha}/L_{\text{bH}\alpha}$ ratios of Composites are consistent with a roughly equal AGN and host contribution to $L_{\text{nH}\alpha}$. In the robust SFs, the host contribution is twice the AGN contribution. An intermediate ratio is seen in the non-robust SFs.

A similar effect is expected in $L_{\text{UV}}/L_{\text{bH}\alpha}$, as star formation will contribute only to L_{UV} . Indeed, the mean $L_{\text{UV}}/L_{\text{bH}\alpha}$ of Composites and robust SFs is 50% higher than in the respective matched group (25% difference in the non robust SFs). Is the observed increase in $L_{\text{UV}}/L_{\text{bH}\alpha}$ consistent with the observed increase in $L_{\text{nH}\alpha}/L_{\text{bH}\alpha}$? Star forming galaxies have a mean $L_{\text{UV}}/L_{\text{nH}\alpha} = 120$ (Kennicutt & Evans 2012). The Composites show an increase of 0.15 in $L_{\text{nH}\alpha}/L_{\text{bH}\alpha}$, and are thus expected to show an increase of $120 \times 0.15 = 18$ in $L_{\text{UV}}/L_{\text{bH}\alpha}$, which is indeed observed (54 from 36, Table 4). The robust SF group show an increase of 0.3 in $L_{\text{nH}\alpha}/L_{\text{bH}\alpha}$, and are thus expected to show an increase of 36 in $L_{\text{UV}}/L_{\text{bH}\alpha}$, which is 50% larger compared to the observed rise of 22. However, the difference is probably consistent within the larger uncertainties in this group. In the non robust SF group the expected rise in $L_{\text{UV}}/L_{\text{bH}\alpha}$ is 12, versus an observed value of 9, again consistent with the uncertainties.

To summarize, the T1 AGN which reside in the Composites and SF regions of the BPT diagrams, also show higher $L_{\text{UV}}/L_{\text{bH}\alpha}$ and $L_{\text{nH}\alpha}/L_{\text{bH}\alpha}$ ratios, compared to pure-AGN. In addition, the ratio of the increase in $L_{\text{nH}\alpha}$ and in L_{UV} is consistent with $L_{\text{UV}}/L_{\text{nH}\alpha}$ observed in star forming galaxies. Thus, AGN powered by accretion onto a massive BH do not produce SF or Composite line ratios, and measurements of such line ratios in AGN implies host contamination.

Could host contamination also affect line ratios within the pure-AGN regime? Could some of the spread in the BPT diagrams, also within the pure-AGN regime, be caused by host contamination? Figure 11 presents the mean BPT positions of T1s binned by $L_{\text{UV}}/L_{\text{bH}\alpha}$. We split the T1 sample to $L_{\text{bH}\alpha} < 10^{42} \text{ erg s}^{-1}$ (upper panels), and $L_{\text{bH}\alpha} > 10^{42} \text{ erg s}^{-1}$ (lower panels). The luminosity cut is set where the host contribution to L_{UV} starts to be significant (Paper I). At $L_{\text{bH}\alpha} > 10^{42} \text{ erg s}^{-1}$, objects within the $L_{\text{UV}}/L_{\text{bH}\alpha} \leq 40$ bins have similar mean positions, but the highest bin $L_{\text{UV}}/L_{\text{bH}\alpha} = 80$ is shifted towards the Composite region. A similar behaviour is observed at $L_{\text{bH}\alpha} < 10^{42} \text{ erg s}^{-1}$. Objects within the $L_{\text{UV}}/L_{\text{bH}\alpha} \leq 30$ bins have similar mean positions, but the $L_{\text{UV}}/L_{\text{bH}\alpha} = 90$ bin is shifted towards the Composite region. The highest bin here has $L_{\text{UV}}/L_{\text{bH}\alpha} = 200$, and its mean position is within the Composite region. Thus, not only that Composite AGN

have a higher mean $L_{\text{UV}}/L_{\text{bH}\alpha}$, as found earlier, also the highest $L_{\text{UV}}/L_{\text{bH}\alpha}$ AGN are on average composite in nature. Therefore, the excess UV, seen in low luminosity AGN, likely arises from star formation in the host, as suggested in Paper I, based on the pure AGN SED.

In addition, AGN within the ‘pure-AGN’ BPT regime can also be affected by host contamination, in particular when getting close to the Ke06 line. Narrow emission lines, powered purely by accretion, likely produces a smaller dispersion than observed in the BPT plots.

8 THE IONIZING SPECTRUM SEEN BY THE NLR

8.1 α_{ox} as a measure of the ionizing spectrum slope

What produces the scatter in the BPT plots? Possible parameters are the ionizing spectral slope and the ionization parameter (e.g. Groves et al. 2004). Below we test this explanation by exploring the dependence of the BPT positions on α_{ox} , the power law slope interpolated from L_{UV} and L_{X} . We use the 752 T1 objects that were observed by GALEX and have $L_{\text{bH}\alpha} > 10^{42.5} \text{ erg s}^{-1}$, to avoid host contamination of the UV. These T1 objects are divided into bins of α_{ox} with width of 0.25. Figure 12 shows the mean and scatter of the BPT-[O I] positions of the different α_{ox} bins. We use the BPT-[O I] panel since it is most sensitive to the ionizing slope (Groves et al. 2004). The X-ray detection rates are 77%, 73%, 67% and 29%, for the $\alpha_{\text{ox}} = -1.2, -1.4, -1.6$ and -1.8 bins, respectively. The UV detection rate is 60% for the $\alpha_{\text{ox}} = -1.2$ bin, and $> 95\%$ in the other bins. Upper limits are used when a detection is not available, so the true α_{ox} of the $\alpha_{\text{ox}} = -1.8$ bin is likely < -1.8 , while the true α_{ox} of the $\alpha_{\text{ox}} = -1.2$ bin is likely > -1.2 .

For comparison, Fig. 12 also shows the expected BPT-[O I] position for ionizing spectra with different slopes and for different ionization parameters, taken from Fig. 1d in Groves et al. (2004), which assume a density of 1000 cm^{-3} and $Z = 2 Z_{\odot}$. Clearly, the observed mean position is independent of the mean observed α_{ox} , in sharp contrast with the models which predict a strong dependence. This discrepancy may either indicate that α_{ox} is not a good indicator of the ionization slope at the EUV, or it may indicate that the dispersion is produced by another parameter, such as Z . Another mechanism that can produce a dispersion in α_{ox} , with no effect on the BPT positions, is dust along the line of sight (Paper I). Normal dust has a higher absorption at UV wavelengths than at X-ray wavelengths. If this dust is located beyond the NLR, the NLR will see the intrinsic ionizing spectrum, and the BPT ratios will not be affected.

8.2 The effect of dust on the ionizing spectrum

Some AGN appear to be dust reddened based on their SED (e.g. Richards et al. 2003). In Paper I, we found that the $L_{\text{UV}}/L_{\text{bH}\alpha}$ distribution at the high luminosity end of the T1 sample is at least partially due to dust reddening along the line of sight. In particular, objects with $L_{\text{UV}}/L_{\text{bH}\alpha} < 30$ show a correlation such that redder optical slopes go with a decreasing $L_{\text{UV}}/L_{\text{bH}\alpha}$. A possible correlation between the reddening and $L_{\text{X}}/L_{\text{AGN}}$ suggested that this dust resides on host galaxy scales, beyond the NLR. This suggestion can now be tested using Fig. 11, which shows the mean BPT positions by $L_{\text{UV}}/L_{\text{bH}\alpha}$. The mean positions of the $L_{\text{UV}}/L_{\text{bH}\alpha} = 40, 10, 4, 1$ bins are all similar to each other, in both high luminosity T1s (lower row) and low luminosity T1s (upper row). If the dust resides inside

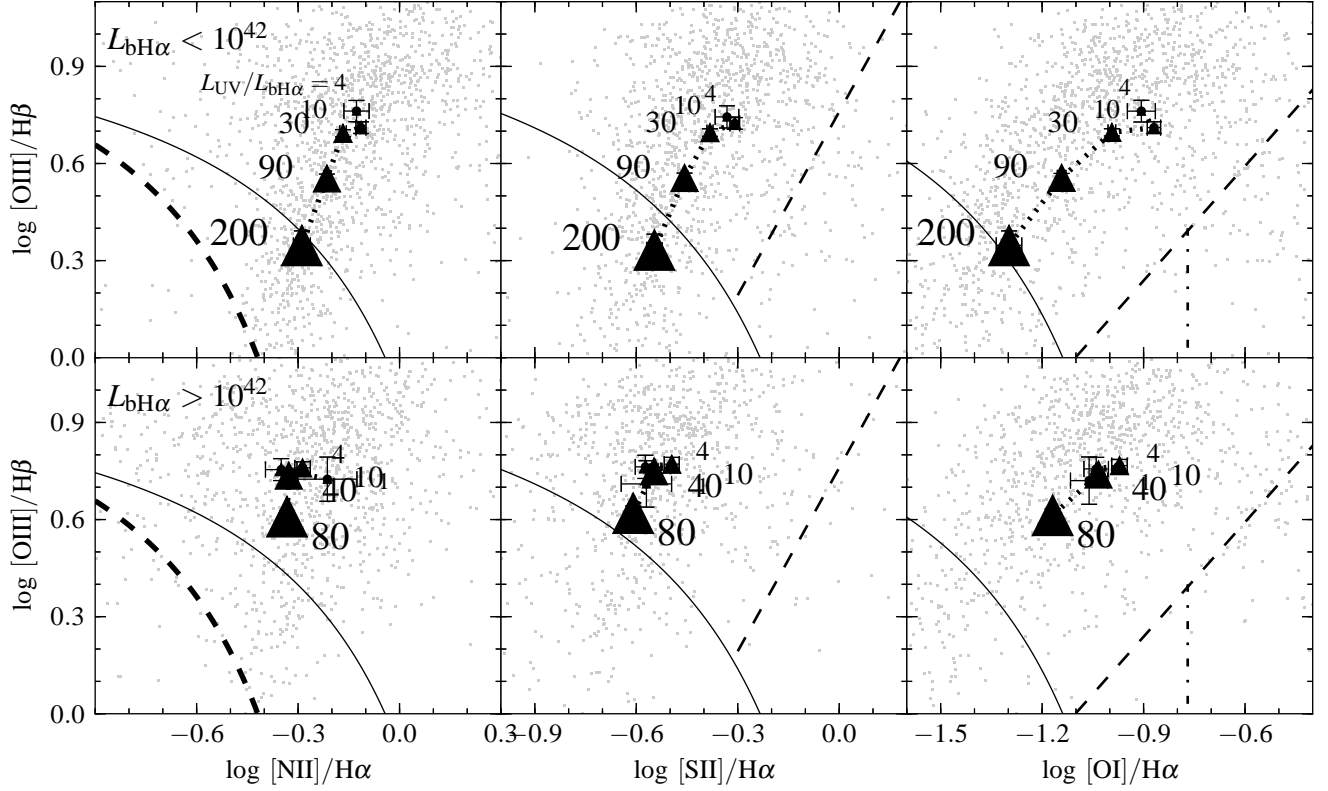


Figure 11. The mean BPT positions by $L_{UV}/L_{bH\alpha}$, for low and high luminosity T1s. Mean positions of 0.5 decade $L_{UV}/L_{bH\alpha}$ bins are denoted by triangles, with marker size increasing with $L_{UV}/L_{bH\alpha}$ (mean value noted). The error bars indicate the uncertainty in the mean position. Only bins with > 10 objects are shown. The positions of individual objects are shown as gray dots. The solid, dashed and dashed-dot classification lines are as in Fig. 2. **Top panels** T1s with $\log L_{bH\alpha} < 42$. The mean position of objects with $L_{UV}/L_{bH\alpha} = 90$ and 200 are offset towards the composite region, indicating the excess UV originates from star formation in the host galaxy. **Bottom panels** T1s with $\log L_{bH\alpha} > 42$. The $L_{UV}/L_{bH\alpha} = 40, 10, 4, 1$ bins have similar mean BPT positions, indicating a similar intrinsic ionizing spectrum at these different $L_{UV}/L_{bH\alpha}$. Therefore, if $L_{UV}/L_{bH\alpha} < 40$ indicates dust extinction (Paper I), the extinguishing dust resides on scales larger than the NLR.

the NLR, then the NLR in objects with a low $L_{UV}/L_{bH\alpha}$ is illuminated by a modified ionizing SED, which will shift their mean BPT position. The complete lack of a trend in BPT position with reddening suggests that the NLR illumination is not modified, and therefore the extinguishing dust resides on scales larger than the NLR.

9 CONCLUSIONS

The narrow line ratios of type 2 AGN have been extensively explored, in particular based on the SDSS sample. Here we present a similar analysis of the T1 sample, the first large (3175 objects) sample of type 1 AGN (Paper I). The T1 sample extends to luminosities well below the SDSS quasar sample, and thus in contrast with quasars, where the narrow lines are generally difficult to measure, here a significant fraction of the objects have strong narrow lines (Paper II). This allows reliable analysis of the narrow line ratios for most objects, as done in type 2 AGN. We find the following:

- (i) The luminosities of all measured narrow lines, $H\alpha$, $H\beta$, $[O III]$, $[N II]$, $[S II]$, $[O I]$, show a Baldwin relation relative to the broad $H\alpha$ luminosity, $L_{line} \propto L_{bH\alpha}^\alpha$, with $\alpha = 0.66, 0.67, 0.72, 0.54, 0.53, 0.63$, respectively (Paper II, and above).
- (ii) About 20% of the T1 AGN have line ratios within the ‘Composite’

and ‘SF’ regions of the BPT diagrams. These line ratios are not powered by accretion onto a massive BH, as these objects also show higher $L_{nH\alpha}/L_{bH\alpha}$ and $L_{UV}/L_{bH\alpha}$ emission. The excess $L_{nH\alpha}$ and L_{UV} is consistent with the ratio expected from SF in the host galaxy, and indicates the line emission in these objects is mostly excited by SF, rather than by the AGN.

- (iii) The other 80% of the T1 AGN, which reside within the BPT AGN region, are offset to lower $[N II]/H\alpha$ and $[S II]/H\alpha$ luminosity ratios, compared to type 2 AGN. This offset is a selection effect, as T1 AGN selected only from the SDSS galaxy sample, as the type 2 AGN are, are not offset. The offset is produced by the T1 point like objects, selected from the SDSS quasar sample, which extend to higher L_{AGN}/L_* . The T2 sample is selected against such objects, and such objects are offset to lower $[N II]/H\alpha$ and $[S II]/H\alpha$.
- (iv) The $[N II]/H\alpha$ and $[N II]/[S II]$ ratios increase with host mass, which suggest a mass-metallicity relation in AGN hosts, as observed in quiescent galaxies. In contrast $[N II]/H\alpha$ decreases with L_{AGN} , but $[N II]/[S II]$ is independent of L_{AGN} , which indicates there is no direct L_{AGN} -metallicity relation.
- (v) At a fixed L_{bol} and L/L_{Edd} , objects with a higher $[N II]/H\alpha$ also have higher broad Fe II luminosity, suggesting the broad line metallicity is also related to the host mass. This may be an additional independent effect to the L/L_{Edd} -metallicity relation, suggested in earlier studies to explain some of the eigenvector 1 relations.

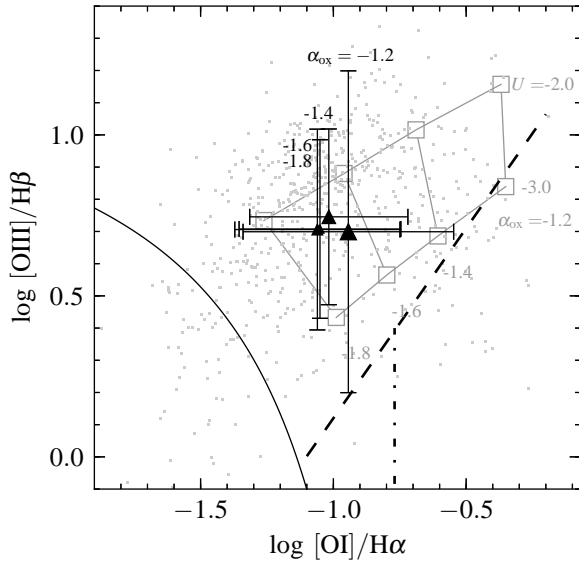


Figure 12. The mean BPT-[O I] positions of the T1 sample, for different α_{ox} . The solid, dashed and dashed-dot classification lines are as in Fig. 2. To avoid host contamination of L_{UV} , only T1 objects with $L_{bH\alpha} > 10^{42.5}$ erg s $^{-1}$ are used (gray dots). The mean position and scatter of each α_{ox} bin is marked by a triangle with error bars (mean α_{ox} noted). For comparison, the expected BPT position for ionizing spectra with different slopes and different $\log U$ are marked (values from Groves et al. 2004). The mean BPT positions of the T1 objects do not follow the trend expected if the slope of the ionizing spectrum is α_{ox} . Either α_{ox} does not represent the EUV spectral slope, or other parameters, such as metallicity, ionization parameters and density control the scatter.

- (vi) The fraction of AGN which are LINERs increases from ~ 0 at $L/L_{Edd} = 10^{-2}$ to ~ 1 at $L/L_{Edd} = 10^{-4}$. The T1 and T2 samples show a similar fraction at a given L/L_{Edd} , indicating the LINER phenomena is unrelated to the presence of an observable BLR. However, the T1 sample terminates at $L/L_{Edd} \sim 10^{-3}$, either due to a physical effect or due to selection effects, and thus LINERs constitute only $\sim 4\%$ of the T1 sample, but $\sim 50\%$ of the T2 sample.
- (vii) The BPT position is unaffected by the value of $L_{UV}/L_{bH\alpha}$ for values < 30 , which provide a measure of the foreground dust extinction (Paper I). This suggests that the ionizing continuum observed at the NLR is unaffected by dust extinction, and the dust likely resides on the host galaxy scale.
- (viii) The BPT position is unaffected by the observed α_{ox} . Models show there is a strong dependence of the BPT position on the ionizing continuum slope. This suggests that α_{ox} is not a good indicator of the EUV ionizing spectrum slope, or that other parameters, such as metallicity, density, and ionization parameter, dominate the scatter in the BPT plots.

We thank Dan Maoz and Hagai Netzer for helpful suggestions and comments. We thank God for finishing this work.

REFERENCES

Abazajian, K., Adelman-McCarthy, J. K., Agüeros, M. A., et al. 2004, *AJ*, 128, 502
 Abazajian, K. N., et al. 2009, *ApJS*, 182, 543
 Adelman-McCarthy, J. K., Agüeros, M. A., Allam, S. S., et al. 2008, *ApJS*, 175, 297

Annibali, F., Bressan, A., Rampazzo, R., et al. 2010, *A&A*, 519, A40
 Baldwin, J. A. 1977, *ApJ*, 214, 679
 Baldwin, J. A., Phillips, M. M., & Terlevich, R. 1981, *PASP*, 93, 5 (BPT)
 Baldwin, J. A., Ferland, G. J., Korista, K. T., Hamann, F., & LaCluyzé, A. 2004, *ApJ*, 615, 610
 Barth, A. J., Greene, J. E., & Ho, L. C. 2008, *AJ*, 136, 1179
 Boroson, T. A., & Green, R. F. 1992, *ApJS*, 80, 109
 Brinchmann, J., Charlot, S., White, S. D. M., Tremonti, C., Kauffmann, G., Heckman, T., & Brinkmann, J. 2004, *MNRAS*, 351, 1151
 Bruzual, G., & Charlot, S. 2003, *MNRAS*, 344, 1000
 Buttiglione, S., Capetti, A., Celotti, A., et al. 2010, *A&A*, 509, A6
 Cardelli, J. A., Clayton, G. C., & Mathis, J. S. 1989, *ApJ*, 345, 245
 Cohen, R. D. 1983, *ApJ*, 273, 489
 Croom, S. M., Smith, R. J., Boyle, B. J., et al. 2001, *MNRAS*, 322, L29
 Croom, S. M., Rhook, K., Corbett, E. A., et al. 2002, *MNRAS*, 337, 275
 De Breuck, C., Röttgering, H., Miley, G., van Breugel, W., & Best, P. 2000, *A&A*, 362, 519
 Dietrich, M., Crenshaw, D. M., & Kraemer, S. B. 2005, *ApJ*, 623, 700
 Fukugita, M., Ichikawa, T., Gunn, J. E., Doi, M., Shimasaku, K., & Schneider, D. P. 1996, *AJ*, 111, 1748
 Gaskell, C. M., Goosmann, R. W., Antonucci, R. R. J., & Whysong, D. H. 2004, *ApJ*, 616, 147
 Greene, J. E., & Ho, L. C. 2007, *ApJ*, 670, 92
 Groves, B. A., Dopita, M. A., & Sutherland, R. S. 2004, *ApJS*, 153, 75
 Groves, B. A., Heckman, T. M., & Kauffmann, G. 2006, *MNRAS*, 371, 1559
 Gültekin, K., Richstone, D. O., Gebhardt, K., et al. 2009, *ApJ*, 698, 198
 Hamann, F., & Ferland, G. 1993, *ApJ*, 418, 11
 Hamann, F., & Ferland, G. 1999, *ARA&A*, 37, 487
 Hao, L., Strauss, M. A., Tremonti, C. A., et al. 2005, *AJ*, 129, 1783
 Heckman, T. M. 1980, *A&A*, 87, 152
 Heckman, T. M., Kauffmann, G., Brinchmann, J., et al. 2004, *ApJ*, 613, 109
 Husemann, B., Wisotzki, L., Jahnke, K., & Sánchez, S. F. 2011, *A&A*, 535, A72
 Ho, L. C., Filippenko, A. V., & Sargent, W. L. W. 1997a, *ApJS*, 112, 315 (Ho97)
 Ho, L. C., Filippenko, A. V., Sargent, W. L. W., & Peng, C. Y. 1997b, *ApJS*, 112, 391
 Ho, L. C. 2002, *Issues in Unification of Active Galactic Nuclei*, ed. Maiolino, R., Marconi, A., Nagar, N., p. 165
 Ho, L. C. 2008, *ARA&A*, 46, 475
 Hönig, S. F., Smette, A., Beckert, T., et al. 2008, *A&A*, 485, L21
 Iwamuro, F., Motohara, K., Maihara, T., et al. 2003, *ApJ*, 598, 178
 Kauffmann, G., et al. 2003, *MNRAS*, 346, 1055 (Ka03)
 Kauffmann, G., Heckman, T. M., White, S. D. M., et al. 2003b, *MNRAS*, 341, 33
 Kauffmann, G., Heckman, T. M., White, S. D. M., et al. 2003c, *MNRAS*, 341, 54
 Kennicutt, R. C., & Evans, N. J. 2012, *ARA&A*, 50, 531
 Keremdjiev, M., Hao, L., & Charmandaris, V. 2009, *ApJ*, 690, 1105

- Kewley, L. J., Dopita, M. A., Sutherland, R. S., Heisler, C. A., & Trevena, J. 2001, *ApJ*, 556, 121 (Ke01)
- Kewley, L. J., Groves, B., Kauffmann, G., & Heckman, T. 2006, *MNRAS*, 372, 961 (Ke06)
- Kraemer, S. B., Ho, L. C., Crenshaw, D. M., Shields, J. C., & Filippenko, A. V. 1999, *ApJ*, 520, 564
- Laor, A., Fiore, F., Elvis, M., Wilkes, B. J., & McDowell, J. C. 1997, *ApJ*, 477, 93
- Laor, A. 2003, *ApJ*, 590, 86
- Laor, A., & Davis, S. W. 2011, *MNRAS*, 417, 681
- Lequeux, J., Peimbert, M., Rayo, J. F., Serrano, A., & Torres-Peimbert, S. 1979, *A&A*, 80, 155
- Ludwig, R. R., Greene, J. E., Barth, A. J., & Ho, L. C. 2012, *ApJ*, 756, 51
- Magorrian, J., et al. 1998, *AJ*, 115, 2285
- Maoz, D., Nagar, N. M., Falcke, H., & Wilson, A. S. 2005, *ApJ*, 625, 699
- Maoz, D. 2007, *MNRAS*, 377, 1696
- Martin, D. C., et al. 2005, *ApJ*, 619, L1
- Nagao, T., Marconi, A., & Maiolino, R. 2006a, *A&A*, 447, 157
- Nagao, T., Maiolino, R., & Marconi, A. 2006b, *A&A*, 447, 863
- Netzer, H., Lutz, D., Schweitzer, M., et al. 2007, *ApJ*, 666, 806
- Richards, G. T., Fan, X., Newberg, H. J., et al. 2002, *AJ*, 123, 2945
- Richards, G. T., et al. 2003, *AJ*, 126, 1131
- Rodríguez-Ardila, A., Binette, L., Pastoriza, M. G., & Donzelli, C. J. 2000, *ApJ*, 538, 581
- Schlegel, D. J., Finkbeiner, D. P., & Davis, M. 1998, *ApJ*, 500, 525
- Shemmer, O., & Netzer, H. 2002, *ApJ*, 567, L19
- Shemmer, O., Netzer, H., Maiolino, R., et al. 2004, *ApJ*, 614, 547
- Shen, Y., Richards, G. T., Strauss, M. A., et al. 2011, *ApJS*, 194, 45
- Shields, G. A., Ludwig, R. R., & Salvander, S. 2010, *ApJ*, 721, 1835
- Stern, J., & Laor, A. 2012a, *MNRAS*, 423, 600 (Paper I)
- Stern, J., & Laor, A. 2012b, *MNRAS*, 426, 2703 (Paper II)
- Storchi-Bergmann, T., Schmitt, H. R., Calzetti, D., & Kinney, A. L. 1998, *AJ*, 115, 909
- Strauss, M. A., et al. 2002, *AJ*, 124, 1810
- Telfer, R. C., Zheng, W., Kriss, G. A., & Davidsen, A. F. 2002, *ApJ*, 565, 773
- Tremonti, C. A., Heckman, T. M., Kauffmann, G., et al. 2004, *ApJ*, 613, 898
- van der Marel, R. P., & Franx, M. 1993, *ApJ*, 407, 525
- van Zee, L., Salzer, J. J., & Haynes, M. P. 1998, *ApJ*, 497, L1
- Veilleux, S., & Osterbrock, D. E. 1987, *ApJS*, 63, 295 (VO)
- Verner, E., Bruhweiler, F., Verner, D., Johansson, S., & Gull, T. 2003, *ApJ*, 592, L59
- Vernet, J., Fosbury, R. A. E., Villar-Martín, M., et al. 2001, *A&A*, 366, 7
- Véron-Cetty, M.-P., Véron, P., & Gonçalves, A. C. 2001, *A&A*, 372, 730
- Voges, W., et al. 1999, *A&A*, 349, 389
- Wang, J., Wei, J. Y., & Xiao, P. F. 2009, *ApJ*, 693, L66
- Wang, J., & Wei, J. Y. 2010, *ApJ*, 719, 1157
- Winter, L. M., Lewis, K. T., Koss, M., et al. 2010, *ApJ*, 710, 503
- Xiao, T., Barth, A. J., Greene, J. E., et al. 2011, *ApJ*, 739, 28
- Yip, C. W., et al. 2004, *AJ*, 128, 585
- Zheng, W., Kriss, G. A., Telfer, R. C., Grimes, J. P., & Davidsen, A. F. 1997, *ApJ*, 475, 469

Appendices

APPENDIX A: MEAN SPECTRA

In §§3 – 5, we show that the distribution of $[\text{N II}]/\text{H}\alpha$ in the T1 sample shifts to lower values with increasing $L_{\text{bH}\alpha}$. To exclude the possibility that this trend is an artifact of our deblending algorithm, we examine the mean spectra at different $L_{\text{bH}\alpha}$ and Δv .

We divide the T1 objects with $[\text{O III}]/\text{H}\beta > 5$ to bins of 0.3 dex in Δv and one decade in $L_{\text{bH}\alpha}$. For each bin, we derive the host-subtracted mean spectrum, as described in §5.3.2. These mean spectra are plotted in Figure A1, with $L_{\text{bH}\alpha}$ increasing from bottom to top, and Δv increasing from left to right. The thin black line in each panel shows the relevant mean spectrum in the L_λ vs. velocity v plane, centered on $\text{H}\alpha$. To enhance the contrast between different NLR and BLR components, we also plot the same mean spectrum centered on $\text{H}\beta$ (thick gray line), with the L_λ of the $\text{H}\beta$ region fit to the L_λ of the $\text{H}\alpha$ region. The fit is performed by a least square minimization of two parameters a and b so that

$$L_\lambda(v_{\text{H}\alpha}) \approx a \times L_\lambda(v_{\text{H}\beta}) + b \quad (\text{A1})$$

for all v in the ranges $-3000 < v < -1000 \text{ km s}^{-1}$, $-200 < v < 450 \text{ km s}^{-1}$ and $1600 < v < 3000 \text{ km s}^{-1}$. The v ranges for the fit are chosen to avoid the $[\text{N II}]$ lines. The best fit coefficient a is between 2.7 and 4 in all panels.

The decrease in $[\text{N II}]/\text{H}\alpha$ with increasing $L_{\text{bH}\alpha}$ is clear in the $\Delta v = 2800, 5200$, and 9600 km s^{-1} columns, confirming the trend found on single objects in §§3–5.

APPENDIX B: BPT BY M_{BH} AND M_*

Figures B1 and B2 show the BPT positions of the T1 sample, divided by M_{BH} and M_* , in the same format as Figures 3–5 above. In Fig. B2, only the 91% of T1 objects with a reliable estimate of M_* (§2.3.1) are shown.

With decreasing M_{BH} the fraction of T1s classified as Composites and SFs increases, indicating an increase in the relative amount of host contribution to the NLR (§7). Since the SDSS is a flux limited sample, T1s with low M_{BH} , and therefore low bulge mass, are preferentially selected from disk dominated galaxies (see Fig. 16 in Paper I). Disks have a relatively large specific star formation rate, which may cause the observed shift in the BPT positions.

With decreasing M_* , an increasing fraction of objects are offset to low $[\text{N II}]/\text{H}\alpha$ values, as found by Groves et al. (2006) on a type 2 AGN sample. This trend is consistent with the $M_* - Z$ relation of quiescent galaxies (Lequeux et al. 1979, and citations thereafter).

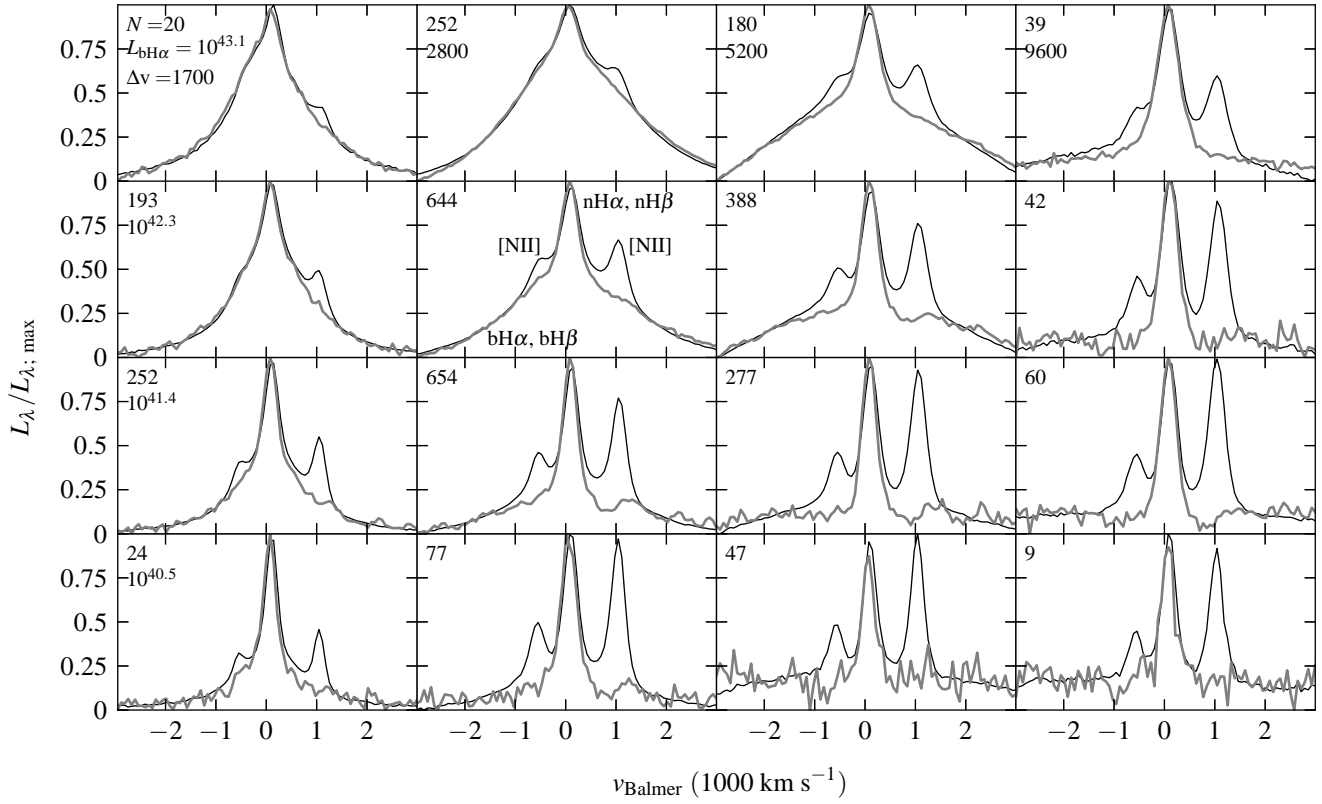


Figure A1. Mean host-subtracted spectra of the $[\text{O III}]/\text{H}\beta > 5$ T1 objects, near H α and near H β , at different $L_{\text{bH}\alpha}$ and Δv . Each panel shows the mean spectrum of T1 objects with the same Δv and the same $L_{\text{bH}\alpha}$ (number of objects noted). The $L_{\text{bH}\alpha}$ increases from bottom to top (mean $L_{\text{bH}\alpha}$ in erg s^{-1} noted in left column), and Δv increases from left to right (mean Δv in km s^{-1} noted in top row). The thin black line plots the mean spectrum centered around H α . To enhance the contrast between different NLR and BLR components, we also plot the mean spectrum centered around H β , with the L_λ adjusted to fit the L_λ of the H α region (thick gray line). In the $\Delta v = 2800, 5200$, and 9600 km s^{-1} columns, the $[\text{N II}]/\text{H}\alpha$ ratio clearly decreases with increasing $L_{\text{bH}\alpha}$.

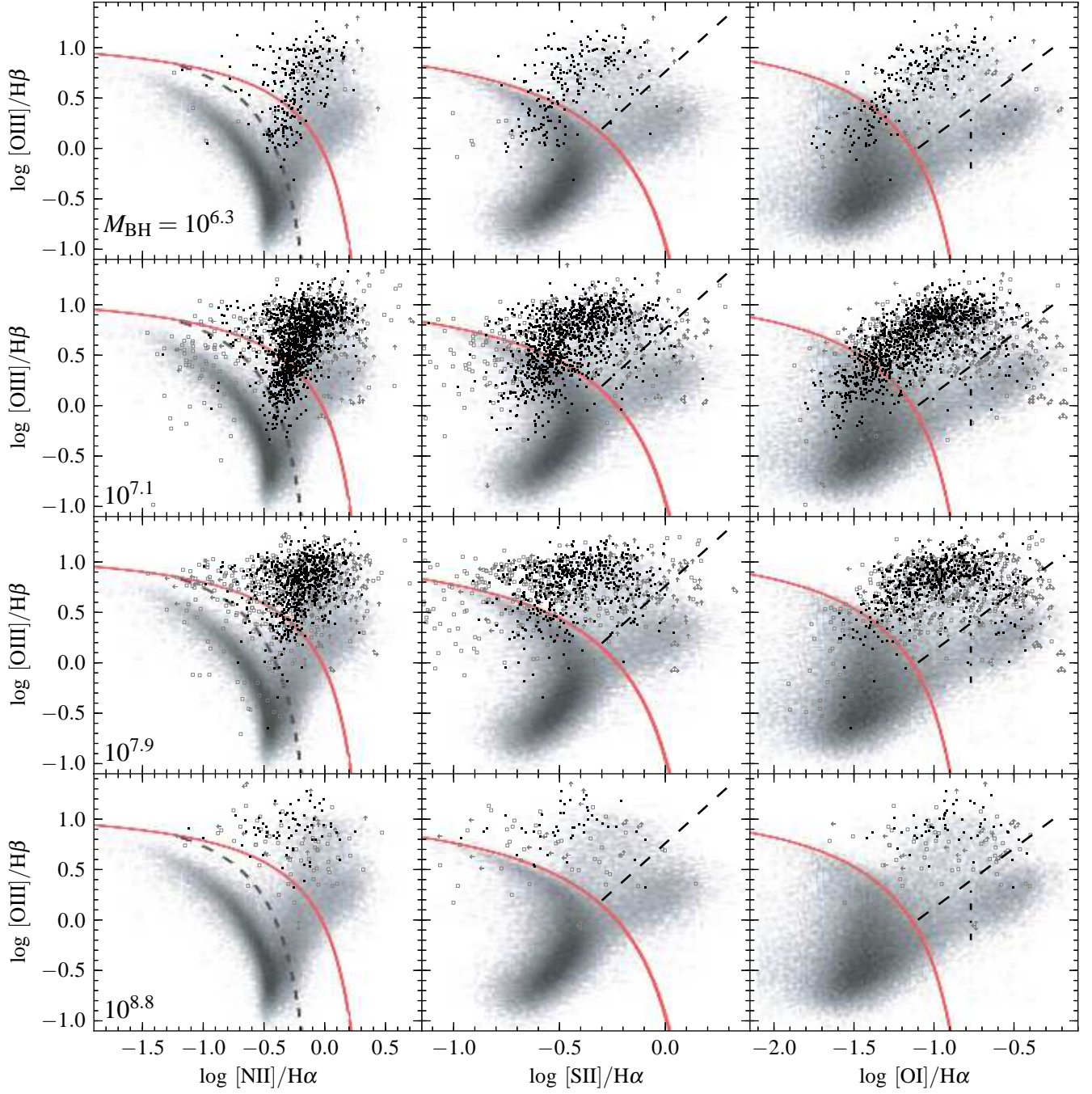


Figure B1. As in Fig. 3, for the dependence of BPT position on M_{BH} . In each row, T1 AGN from a given decade-wide bin in M_{BH} are plotted (mean M_{BH} noted, in M_{\odot}). The frequency of composites and SFs decreases with increasing M_{BH} , from 32% at $\log M_{\text{BH}} = 6.3$, to 23%, 14% and 6% at $\log M_{\text{BH}} = 7.1$, 7.9 and 8.8, respectively.

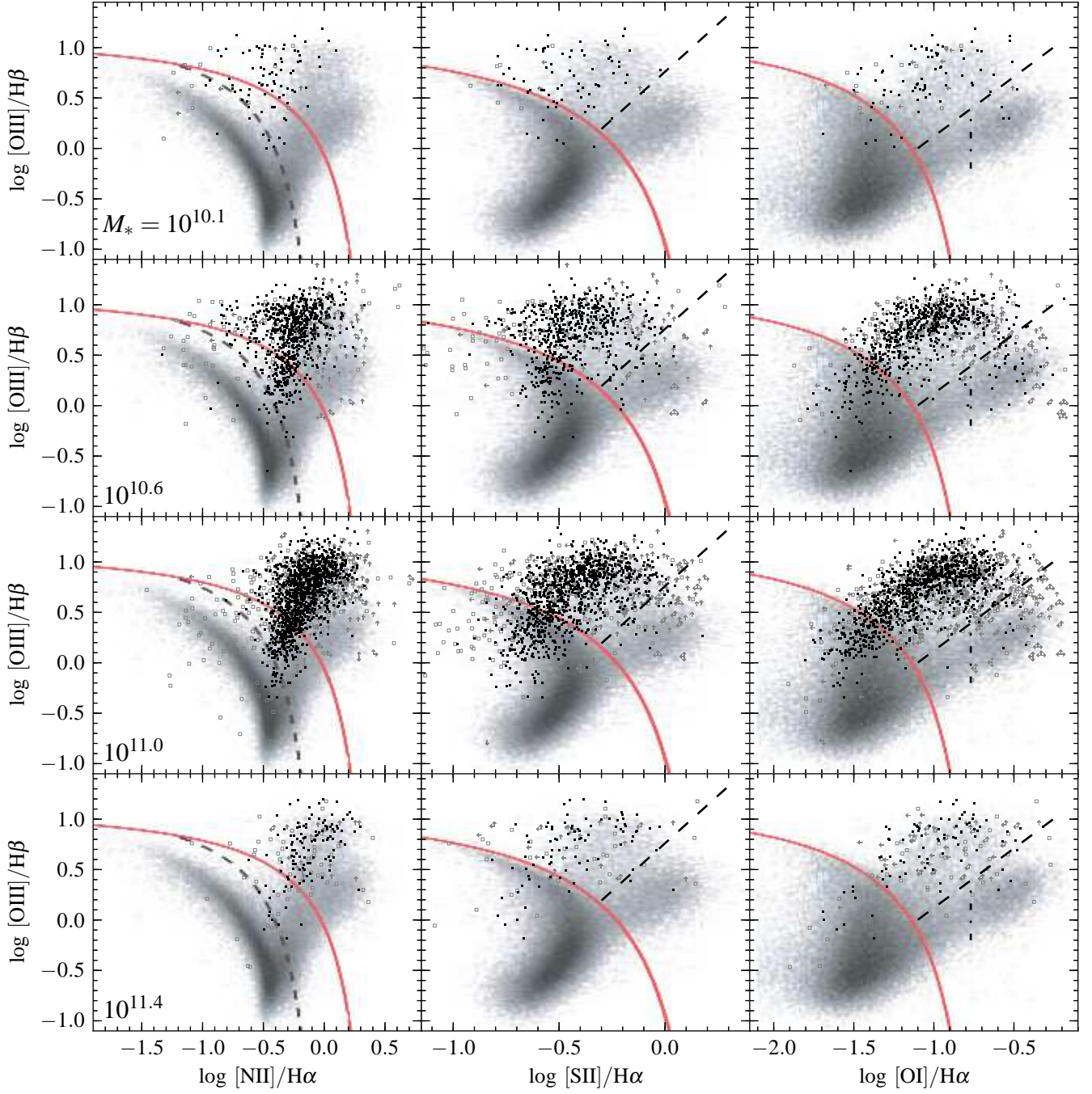


Figure B2. As in Fig. 3, for the dependence of BPT position on M_* . In each row, T1 AGN from a given half decade wide bin in M_* are plotted (mean M_* noted, in M_\odot). With decreasing M_* , an increasing fraction of objects are offset to low $[\text{NII}]/\text{H}\alpha$ values, consistent with the $M_* - Z$ relation of quiescent galaxies.